Composites Part B 284 (2024) 111713

Contents lists available at ScienceDirect

Composites Part B

journal homepage: www.elsevier.com/locate/compositesb

Hydrophilic silsesquioxane nanocages toughened extracellular matrix biomimetic Poly(γ-Glutamic acid) multidimensional self-polymerizable and osteogenic hybrid hydrogel for osteoporotic bone regeneration

Lingli Liu [a,b,c,1], Shiyuan Ma [b,1], Zhisheng Xiao [a,1], Jintao Li [a], Yue Wang [b], Zhihui Lu [b,c,**], Yitao Zhao [a,***], Jinshan Guo [a,b,c,d,*]

[a] Department of Orthopedics, Center for Orthopedic Surgery, Orthopedic Hospital of Guangdong Province, The Third School of Clinical Medicine, Guangdong Provincial Key Laboratory of Bone and Joint Degeneration Diseases, Southern Medical University, The Third Affiliated Hospital of Southern Medical University, Guangzhou, Guangdong, 510630, PR China

[b] Department of Histology and Embryology, NMPA Key Laboratory for Safety Evaluation of Cosmetics, School of Basic Medical Sciences, Southern Medical University, Guangzhou, 510515, PR China

[c] Regenerative Medicine and Tissue Repair Material Research Center, Huangpu Institute of Materials, 88 Yonglong Avenue of Xinlong Town, Guangzhou, 511363, PR China

[d] CAS Key Laboratory of High-Performance Synthetic Rubber and Its Composite Materials, Changchun Institute of Applied Chemistry, Chinese Academy of Sciences, 5625 Renmin Street, Changchun, 130022, PR China

ARTICLE INFO

Handling Editor: Hao Wang

Keywords:
Osteoporotic bone regeneration
Hydrophilic NH_2-T4-POSS
Organic/inorganic hybrid
Multidimensional self-polymerizable hydrogel
Balance immune micro-environment

ABSTRACT

Rapid bone defect regeneration in osteoporotic conditions remains a significant challenge due to the fragile mechanical stability and pathological microenvironment. The absence of bone matrix is the primary characteristic of these defects, and advanced strategies for treating osteoporotic bone defects focus on remodeling the bone matrix's spatial structure and regulating the microenvironment. While many hydrogels have been developed for bone regeneration, their use in repairing osteoporotic bone defects is constrained by deficiencies in shape-adaptivity, weak osteogenic bioactivity, and lack of physiological mechanical support. Herein, a novel bioactive hydrophilic semi-caged NH_2-T4 silsesquioxane (NH_2-T4-POSS) nanocage was developed, which was used to modify γ-polyglutamic acid (γ-PGA) together with dopamine, to give an organic/inorganic hybrid hydrogel PGA-DA&T4 for osteoporotic bone regeneration. The developed PGA-DA&T4 hydrogel possesses favorable injectability, shape-adaptivity, self-healability, and strong antioxidant ability. Benefited from organic/inorganic hybridation and multidimensional molecular interacting mechanism, PGA-DA&T4 exhibites enhanced thermal stability and longer degradation period, unique self-polymerizability, high elasticity, and considerable tissue adhesion ability. In vitro experiments proved that PGA-DA&T4 is biocompatible, and is able to promote cell migration and neovascularization, and possesses favorable immunoregulatory to promote macrophage polarization towards anti-inflammatory M2 phenotype. Furthermore, PGA-DA&T4 has been demonstrated to accelerate osteogenic differentiation and inhibit osteoclastogenesis, thereby promoting the repair of osteoporotic bone defects. Our research successfully developed a novel hybrid γ-PGA hydrogel with therapeutic effects and supplied a promising biomaterial with potential clinical application for repairing osteoporotic bone defects.

1. Introduction

Over the past four decades, there has been a significant increase in the global aging population, resulting in osteoporosis (OP)-related fractures becoming a major global health problem [1]. These fractures pose a serious threat to the lives and well-being of middle-aged and elder human beings. Osteoporosis is a degenerative bone disease characterized by an imbalance between osteogenic and osteoblastic metabolism,

* Corresponding author.
** Corresponding author.
*** Corresponding author.
E-mail addresses: sanlumo12@smu.edu.cn (Z. Lu), zyt36634@163.com (Y. Zhao), jsguo4127@smu.edu.cn (J. Guo).
[1] These authors contribute equally.

https://doi.org/10.1016/j.compositesb.2024.111713
Received 13 March 2024; Received in revised form 5 June 2024; Accepted 8 July 2024
Available online 9 July 2024

resulting in weakened bones with low bone mineral density [2]. This results in various types of fragility fractures that are difficult to heal, significantly impacting the quality of life and increasing mortality in OP patients. Aim to address these challenges, clinicians and researchers have conducted numerous studies to explore more effective therapeutic approaches for fragility fractures. These studies normally focused on issues such as the limited efficacy of traditional medications, side effects of bone grafting, inadequate mechanical support, and immune microenvironmental imbalances [3,4]. However, the complex challenges of fragility fractures require comprehensive strategies to improve outcomes.

The field of tissue engineering has witnessed a progress of biomaterial scaffolds, yet these still face several hurdles, such as suboptimal biocompatibility, an inability to recruit cells and stimulate osteogenic differentiation, compromised mechanical integrity, and inability to meet the clinical requirements for osteoporotic bone defect repair [5,6]. Major obstacles in repairing osteoporotic bone defects include lack of adequate mechanical adaptation and mismatch between osteogenesis and osteoclast resorption, further compounded by an unfavorable microenvironment and pathological inflammatory responses [7]. However, the use of hydrogels as a biomaterial for osteoporotic bone defect therapy is a promising advancement. Hydrogels are highly hydrated and possess commendable biocompatibility, excellent permeability, tunable biodegradability, injectability, and modifiable mechanical strength [8–10]. They are capable of creating a three-demensional network structure similar to the natural extracellular matrix. This makes it an excellent substrate to work with other bioactive components to enhance bone tissue regeneration and reconstruction [11]. Furthermore, hydrogels are endowed with amplified capacity for biological regulation following the introduction of suitable chemical modifications and bioactive factors. With proper design, hydrogels can represent promising materials for bone repair, exhibiting the capacity to modulate inflammation, recruite and proliferate cells and biologic entities, promote angiogenesis, induce osteogenic differentiation, apply biomechanical loads and stimuli at the defect site, and promote biomineralization [12–16].

γ-Polyglutamic acid (γ-PGA), a polypeptide composed of linear polymeric chains of L-glutamic acid, exhibits a structural resemblance to the natural protein-based extracellular matrix (ECM) [17]. γ-PGA possesses commendable biocompatibility and bioactivity, and it can biodegrade into non-toxic amino acid monomers. These attributes have attracted attention for γ-PGA in the fabrication of scaffolds for tissue regeneration and the study of modification methods [18,19]. Despite its potential, γ-PGA encounters difficulties in establishing interaction with solid-state and biological environments, particularly under wet/dynamic conditions. Sub-optimal adhesive properties, lack of gel formation and relatively low mechanical strength are among its inherent limitations. Thus, while γ-PGA has considerable value, it is often employed in a composite role with other polymers rather than as a standalone material for orthopedic applications, an area where functional modification research based on γ-PGA alone is scarce [20].

To achieve the concept of bone matrix biomimicry, it is crucial to execute organic-inorganic hybrid scaffolds [21]. Silicon dioxide, a naturally occurring inorganic substance, has been shown to integrate well with bone tissue *in vivo*. Accumulating evidence implies that silica-incorporated scaffold materials in promoting internal vascularization and are notable for bone regeneration capacities, bolstering osteoblast attachment, and stimulating osteogenic responses [22]. Polyhedral oligomeric silsesquioxanes (POSS) represent one of the smallest known siliceous nanoparticles. They possess atomically precise, cage-like structures with silica cores and versatile functional groups, which have demonstrated a high potential for promoting bone regeneration when applied as bone repair scaffolds [23,24]. This renders them susceptible to modifications with a multitude of organic substituents for enhancing compatibility and functionality via compounding with other polymers [25,26]. Specifically, NH_2-T4 silsesquioxanes (NH_2-T4-POSS), attributed to their semi-cage configuration and hydrophilic nature, are considered prime candidates for engineering nanocomposites. We indicates that hydrogels integrated with NH_2-T4-POSS exhibit excellent cytocompatibility and facilitate the adhesion, migration, proliferation, and osteogenic differentiation of bone marrow stromal cells (BMSCs) [27,28]. Moreover, NH_2-T4-POSS entities can be safely and seamlessly incorporated into polymer matrices as covalent, self-assembling building blocks. This improves the thermal and mechanical properties of the host hydrogels [25,29,30], rendering them advantageous for bone healing applications. Our research collective has previously engineered a citrate-based, tannin-bridged organic/inorganic composite biomaterial that has been demonstrated to facilitate the healing of critical bone defects. The accelerated healing observed is attributed to the combined actions of tannin and citrate constituents [31]. Our findings indicated that fracture regeneration was enhanced by immobilization with bone binders and reduction of comminuted bone fragments. Meanwhile, dopamine exhibited excellent aquatic adhesion and provided a range of functional groups, including catechols, amines, and imines, which are suitable for further chemical modifications [32,33].

In this study, we have employed organic/inorganic hybrid bone repair biomaterials to construct advanced PGA-DA&T4 hydrogels. The hydrogels exhibit exceptional properties, including high adhesion, superior mechanical conductivity, multilayered interoperable topology, and bioactivities. These properties were achieved by modifying the γ-PGA with nano-caged NH_2-T4-POSS siloxanes and dopamine hydrochloride, as shown in Scheme 1. Importantly, the dual modification of NH_2-T4-POSS and dopamine in the multidimensional self-polymerizable hybrid PGA-DA&T4 hydrogels resulted in controlled biodegradability, elastic mechanical behavior, strong adhesion, and enhanced osteoblastic bioactivity. Moreover, the hybrid PGA-DA&T4 hydrogel is designed as a polyinductive scaffold that mimics the natural bone microstructure. The hydrogel can modify the immune microenvironment to promote angiogenesis, osteogenic differentiation, and biomineralization, thereby facilitating the healing of osteoporotic bone defects. The findings of our study provide a novel design strategy and experimental foundation for developing biomimetic materials for the treatment of osteoporotic bone defects that are simpler, more efficient, and safer. These findings have significant clinical value and offer considerable social benefits.

1.1. Experimental part

1.1.1. Materials

N-Hydroxysuccinimide (NHS), 3-hydroxytyramine hydrochloride, 1-ethyl-(3-dimethylaminopropyl) carbodimide hydrochloride (EDC·HCl) were all purchased from Sigma-Aldrich. (3-Aminopropyl)triethoxysilane, dopamine hydrochloride (DA), potassium methylate (CH_3OK), and poly (γ-glutamic acid) sodium salt (γ-PGA) were obtained from Aladdin. All chemicals were used without further purification.

1.2. Preparation and properties of half cage-like NH_2-T4-POSS and hybrid hydrogels (PGA-DA&T4)

NH_2-T4 silsesquioxane (NH_2-T4-POSS) was synthesized via a method described in our previous work [25,26]. Into a 250 mL three-necked round-bottom flask charged with 100 mL isopropanol and 50.0 g (3-aminopropyl)triethoxysilane, 23.4 g potassium methylate (CH_3OK) in 19.8 mL distilled water was added dropwise. The mixture was stirred at 50 °C for 8 h, and then the solvent was removed via rotary evaporation. After washing with acetone and fully removing the solvent followed by precipiting in methanol and recrystallized in acetone, purified NH_2-T4-POSS was obtained.

FTIR (KBr): 3415 (w; N–H), 2986 (w; C–H), 1576 (w; N–H), 1463 (s; –CH_2), 1255 (s; –C–N), 1084 (s; Si–O–Si), 802 (s; Si–C). **^{1}H-NMR** (D_2O): $SiO_{1.5}C\mathbf{H}_2$ (a) $C\mathbf{H}_2$ (b) and $C\mathbf{H}_2N$ (c), a: 2.57 ppm, 2H; b: 1.43 ppm, 2H; c: 0.41 ppm, 2H. **^{13}C-NMR** (δ, ppm): $SiO_{1.5}\mathbf{C}H_2$ (1) $\mathbf{C}H_2$ (2) and $\mathbf{C}H_2N$ (3), 1: 10.77 ppm; 2: 24.25 ppm; 3: 43.01 ppm; **^{29}Si-NMR** (δ, ppm): −67.8.

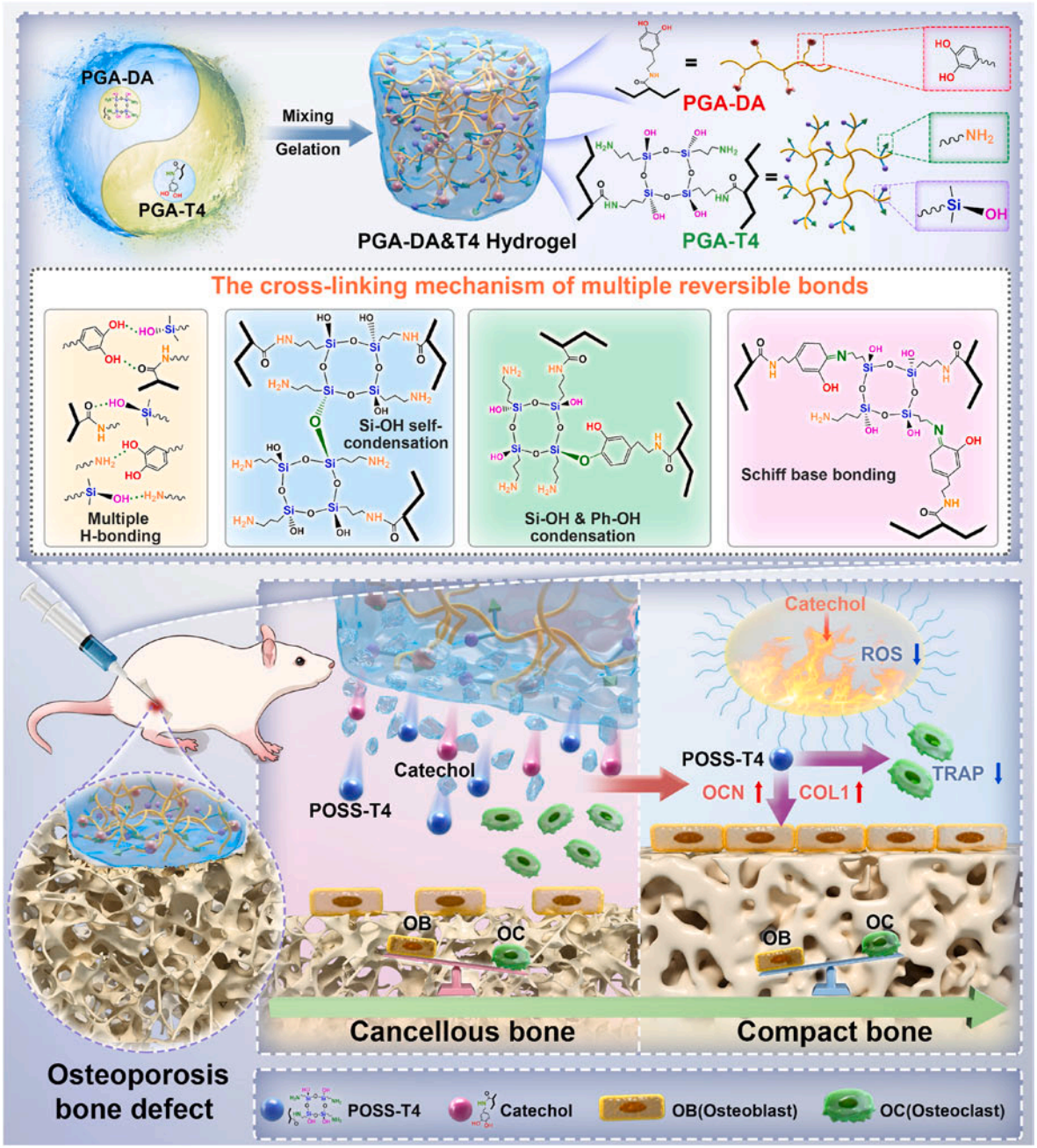

Scheme 1. Schematic diagram of silsesquioxanes nanocages-hybrid PGA-DA&T4 hydrogels boosts femoral condylar bone defects repairing in osteoporosis rats.

All NMR samples were dissolved in D_2O.

The synthesis of dopamine grafted γ-PGA (PGA-DA) and NH_2-T4 silsesquioxane modified γ-PGA (PGA-T4) was described detail in Support information 1.1–1.2, respectively. As shown in Scheme 1, component A was made of 30 % wt/v% PGA-DA solution in DI water, which was then mixed with 30 % PGA-T4 component (B) to prepare hybrid hydrogel (V_A/V_B from 3/1 to 1/3). We designed five different hydrogels with various ratios of PGA-DA and PGA-T4, they were named DA&T4-3/1, DA&T4-2/1, DA&T4-1/1, DA&T4-1/2, and DA&T4-1/3. The gelation times for PGA-DA&T4 hydrogels with different component ratios are shown in Table S1. The test methods of general physicochemical, mechanical adhesive properties, *in vitro* degradation and release profiles of γ-PGA and modified PGA hydrogels are shown in Support information 1.3–1.6.

1.3. Cytocompatibility of PGA and modified PGA hydrogels

The cytocompatibility of PGA and modified PGA materials was assessed by cell counting kit-8 (CCK-8, Biosharp) and Live/Dead viability/cytotoxicity kit (Bestbio), using rat bone marrow mesenchymal stem cells (BMSCs, Cyagen, RASMX-01001) as cell models [28,34]. BMSCs were cultured in 96 well plates (100 μL, 1×10^5 cells/mL). The cells were incubated in complete growth medium (minimum essential medium (MEM) with 10 % (v/v) fetal bovine serum (FBS) and 1 % (v/v) antibiotic antimycotic solution (**100** ×)) under the condition of 37 °C, 5 % CO_2 and 95 % relative humidity for 24 h, and 10 μL suspension of PGA, PGA-DA, PGA-T4 or PGA-DA&T4 in sterile PBS (1000, 100, 50, 20 μg/mL), was added. The cells were co-cultured for another 24 h before conducting a CCK-8 assay and measuring the absorbances at 450 nm with a microplate reader. At least 5 parallels were set for each sample and the obtained cell viabilities were averaged. The suspensions of

modified/unmodified PGA with a concentration of 100 μg/mL were used for the Live/Dead study. In each well of 24-well plates, 500 μL BMSC suspension was seeded (1×10^5 cells/mL) and cultured for 24 h. Then add 50 μL of modified/unmodified PGA suspension (100 μg/mL) and incubate the cells for 1, 3, 5 days, followed by Live/Dead assays and staining according to the manufacturer's protocol.

The OD value was measured at a wavelength of 450 nm by an enzyme-linked immunosorbent assay. Cell viability can be calculated by the following formula:

$$\text{Cell viability}\ (\%) = \frac{OD450_1}{OD450_2} \times 100 \quad \text{Eq. (1)}$$

$OD450_1$ represents the OD value of sample group and $OD450_2$ represents the OD value of blank group.

1.4. Scratch and transwell assays

The logarithmicly grown BMSCs were seeded in a 6-well plate with a cell density about 5×10^5 cells/well. After being cultured in a complete growth medium for 24 h, the cells adhered to form monolayer cells, then three vertical marks were drawn by a 200 μL tip, washed with PBS three times to remove floating cells, and then the cells were cultured in the complete growth medium containing with 1/10 (v/v) **10** × degradation product [15]. After incubation for 12 h, the cells were observed and photographed by an inverted microscope, and the cell migration rate was quantitatively analyzed by ImageJ and calculated using the following formula:

$$\text{Migration rate}\ (\%) = \frac{W_i\text{-}W_S}{W_i} \times 100 \quad \text{Eq. (2)}$$

where W_i denotes the initial scratch width at 0 h, and W_s represents the scratch width after culturing for 12 h.

For transwell assay, transwell chambers (Corning, 353097) were put into the wells of 24-well plates, the logarithmicly grown BMSCs in complete growth medium with 1/10 (v/v) **10** × degradation product of unmodified/modified PGA hydrogel with a cell density of 1×10^4 cells/mL were seeded in the chambers (500 μL/chamber) and cultured for 24 h in a 37 °C incubator [33,34]. Then the cells on the upper surface of the chamber were completely removed by wiping with a cotton swab and those on the lower surface were subsequently fixed with 4 % formaldehyde solution for 30 min and stained with crystal violet for 15 min. After staining, the cells were washed with PBS and placed on a glass slide, observed, and photographed under an optical microscope. Then the chamber was immersed in 30 % glacial acetic acid for elution, and the OD value of the solution at 570 nm was measured by enzyme-linked immunosorbent assay to quantify the number of cells.

1.5. In vitro tube formation assay and osteogenic properties of the hydrogels

An *in vitro* angiogenesis experiment was used to verify the angiogenic ability of the hydrogels using human umbilical vein endothelial cells (HUVECs). To each well of a 48-well plate, 100 μL matrigel matrix glue was added and gently shaken to cover the bottom of the well and placed in a 37 °C incubator for more than 1 h. The cells resuspended in a complete medium containing a 10× degradation product at a density of about 5×10^4 cells/mL was added to the well and incubated in a 37 °C, 5 % CO_2 incubator for 12 h. The state of cell tube formation was observed by an inverted microscope and photographed, and the angiogenic ability was quantitatively analyzed by ImageJ and analysis software.

To investigate the osteogenic property of different hydrogels, BMSCs were seeded in the wells of 24-well plates and cultured for 24 h. Then, osteogenic medium (complete growth medium supplemented with 10^{-7} mol/L dexamethasone, 10^{-2} mol/L β-glycerophosphate, and 50 mmol/L L-ascorbic acid) supplemented with **10** × degradation products (1/10 (v/v) to osteogenic medium) of different hydrogel were added (1 mL/well), and the cell were cultured for 7 or 14 days [28]. The medium was changed every two days. For ALP staining, After 7 or 14 days' culture in osteogenic media, alkaline phosphatase (ALP) and Alizarin red S staining, ALP quantitative assay kit.

(Beyotime, P0321) and quantitative polymerase chain reaction (qPCR) were conducted. ALP and Alizarin red S staining was conducted on fixed cells (with 4 % polyformaldehyde (PFA)) following the manufacturer's protocol. The stained cells were visualized and photographed using an inverted fluorescence microscope (Leica DMI4000 B; Leica Microsystems GmbH, Wetzlar, Germany). The qPCR was used to detect the expression of mRNAs of osteogenic-related proteins including ALP, collagen I (COL-1), Runt-related transcription factor 2 (Runx2), and osteopontin (OPN). Total RNA was isolated using a Trizol reagent (Invitrogen, USA). 1000 ng RNA was reverse transcripted using the First Strand cDNA Synthesis Kit (Thermofisher, USA). SYBR green PCR Master Mix (Thermofisher, USA) was used in qPCR with CFX96 Connect Real-Time PCR Detection System (BIO-RAD, USA). ΔΔCt method was applied to calculate the results. The primers used in this study were designed by Primer 3.0 (Table S2).

1.6. Antioxidant activity of composite hydrogels

To a four mL of 100 μM 2,2-diphenyl-1-picrylhydrazyl (DPPH) solution in ethanol, take 0.1g freeze-dried PGA, PGA-DA, PGA-T4, or PGA-DA&T4 samples was added. After incubation under dark for 1 min, the absorbance of the solution at 517 nm (A_s) was measured using a UV–vis spectrophotometer (Shimadzu UV-2550). The untreated DPPH solution was used as the control group and the absorbance (A_c) was also measured. DPPH scavenging percentages were calculated using the following equation:

$$\textit{DPPH scavenging}\ (\%) = \frac{A_s - A_c}{A_c} \times 100 \quad \text{Eq. (3)}$$

The intracellular ROS scavenging capacity of composite hydrogels was evaluated using a 2′, 7′-dichlorodihydrofluorescein diacetate (DCFH-DA) probe using BMSCs. Briefly, BMSCs were seeded in 24-well plates, and incubated at 37 °C for 12 h. PGA (1 mg/mL) or 10× degradation product of PGA-DA, PGA-T4, or PGA-DA&T4 composite hydrogel was added and co-cultured with cells for 4–6 h [28,34]. After 12 h, H_2O_2 (10 μM) was also added and co-cultured with cells for 30 min. Untreated cells and cells treated with 10 μM H_2O_2 only were used as negative and positive controls respectively. Then the culture medium was removed and DCFH-DA (1 μL DCFH-DA solution per mL medium) in serum-free medium was added. After incubation for another 20 min, the cells in the 24-well plates were observed by an inverted fluorescence microscope. Attention should be paid to avoiding light during the experiment.

1.7. Immunoregulatory capacity of composite hydrogels

Immunofluorescence staining was conducted to evaluate the immunoregulatory capacity of composite hydrogels. After being treated with LPS/IL-4 degradation product of composite hydrogel, RAW264.7 seeded on sterilized glass coverslips were fixed by 4 % paraformaldehyde and blocked by 1 % bovine serum albumin (BSA), followed by incubating with primary CD86 and CD206 antibodies at 4 °C overnight. After washing with PBS, the corresponding secondary antibodies were added and incubated at room temperature for 1 h in the dark. Then the cells were washed with sterile PBS, and incubated with 20 μL 4′, 6-diamidino-2-phenylindole (DAPI, Solarbio, Cat# C0065) solution under dark at room temperature for 10 min. Then, the coverslips were placed on glass slides sealed with clear nail polish, and observed by confocal laser scanning microscopy (CLSM, Zeiss, LSM 880). Semi-quantitative analysis was also performed with Image J.

1.8. Macrophage isolation and osteoclast culture

Raw264.7 cells were cultured at 37 °C in 5 % CO_2 for 1 day, then cultured in 500 μL of α-MEM containing 10 % heat-inactivated fetal bovine serum, glutathione-S-transferase-RANKL in 48-well tissue culture plates. After the addition of 10× different hydrogel degradation products, the cells were cultured for another 5 days and fixed and stained for anti-tartrate phosphatase (TRAP) activity using a commercial kit (Sigma 387-A; Sigma-Aldrich, St. Louis, MO). Images were taken using a Nikon Eclipse E400 (Melville, NY) upright microscope. Semi-quantitative analysis was also performed with Image J. Osteoclast were inoculated onto the bone plates at a density of 10^4 cells per plate, and after osteoclasts were induced the bone slices were fixed and washed. The bone slices were incubated for 30 s in 0.5 M NaOH, and the cells were dried with a wet swab; the bone slices were then incubated for 30 min at 37 °C with 50 μg/mL of peroxidase-conjugated wheat Then, the bone slices were incubated with 50 μg/mL peroxidase-conjugated wheat embryo agglutinin (Sigma) for 30 min at 37 °C, and then incubated with 3,3'-diaminobenzidine solution (DAB) for 30 min. Bone plate images were obtained using a Zeiss fluorescence microscope.

1.9. In vivo study

All animal experiments were conducted in compliance with the Animal Experimental Committee of Institute of Biological and Medical Engineering, Guangdong Academy of Sciences (Approval No. 2021013). Forty-eight female Sprague Dawley (SD) rats (8 weeks old) were purchased from the Medical Animal Experiment Center of Southern Medical University and were randomly divided into four groups (12 rats in each group): the blank control group, the PGA group, the PGA-T4 group, and the PGA-DA&T4 group. Firstly, ovariectomy (OVX) debridement was conducted, and after 1 month, the osteoporosis model was established [28]. Femoral condylar defects were then created: the right hind limb of SD rats was shaved, and the rats were anesthetized by injection of sodium pentobarbital (30 mg/kg). Using the patellar ligament as a reference, a 1.5- to 2.0-cm-long incision was made in the lateral femoral condyle parallel to the long axis of the femoral stem. A perforator was then used to create a defect 3.5 mm in diameter and 5 mm deep in the rat femoral condyle. Composite hydrogels (PGA, PGA-T4, and PGA-DA&T4) were then injected into the defect site. Rats were sacrificed 4 and 12 weeks postoperation, and tissues surrounding the treated bone defects were collected for micro-computed tomography (micro-CT) analysis and histological examination.Micro-CT scans of the fixed femoral condyle specimens were performed using a microtomography system (Viva CT80; Scanco Medical AG, Bassersdorf, Switzerland) with a voltage of 50 kV, a current of 145 mA, and a resolution of 30 mm per pixel. X-ray projections were obtained at intervals of 0.72 u, and the scanning angle was rotated by 360 u. To calculate the microtomographic resolution of the fixed femoral condyle specimens in the three groups, a scanning angle of 0.72 u was used. The X-ray projections were obtained at intervals of 0.72 u and the scanning angle was rotated by 360 u. To calculate the bone mineral density (BMD) of the three groups, hollow cylindrical objects of interest (VOI) with diameters of 3.5 mm and 5 mm respectively, were selected for the scanning, and the CT values were corrected to assess the bone regeneration at the site of the defect. Horizontal and vertical two-dimensional (2D) images of the regenerated femoral condyle sections were reconstructed using Mimics Medical 21.0 software. Moreover, at predetermined time points (4 and 12 weeks postoperation), the bone was decalcified with ethylenediaminetetraacetic acid (EDTA) solution (pH 7.4, Solarbio, China) at 37 °C for 1 month, and then histologically examined according to standard protocols. Longitudinal sections of 4 μm were cut in the region of interest using a SP2500 microtome (Leica Microsystems, Wetzlar, Germany). Hematoxylin and eosin (H & E) staining, Masson trichrome staining, TRAP staining, immunohistochemical staining for OCN (Proteintech, 23418-1-AP) and IL-1β (Proteintech, 10806-1-AP) were carried out and the stained sections were visualized by light microscopy (DM 5500B, Leica, Germany). Semi-quantitative analysis of osteoblasts, IL-1β, and OCN positively stained cells was also performed using Image J.

1.10. Statistical analysis

Data were analyzed using SPSS Statistics 25 statistical software. All quantitative results are expressed as mean ± standard deviation (SD). The statistical significance between two sets of data was determined by one-way analysis of variance (ANOVA). Differences were considered statistically significant when * and ** represent $p < 0.05$ and $p < 0.01$, respectively.

2. Results and discussion

2.1. Preparation and characterizations of the γ-PGA and modified PGA hydrogels

As shown in Fig. 1A, comparing to the FT-IR spectrum of PGA, the show up of new peaks at 3321 and 3070 cm^{-1} in the FT-IR spectrum of PGA-DA, which can be assigned to the phenolic hydroxyl and phenyl C–H stretching vibrations of dopamine, confirms the successful introduction of dopamine grafting of PGA-DA. The appearance of the characterized peaks at 6.69–6.76 ppm (peak F), assigned to the protons on benzene ring of dopamine, in the ^{1}H NMR of PGA-DA (Fig. 1B) further confirmed the successful sysnthesis of PGA-DA. The structure of PGA-T4 modified via NH_2-T4-POSS was verified by the appearance of absorption peaks at 1025 and 845 cm^{-1} in the FT-IR spectrum of PGA-T4 (Fig. 1A), attributed to Si–O–Si and Si–C stretching vibration peaks (Fig. S1A). The formation of Schiff base bonds between the amino group NH_2-T4-POSS and oxidized dopamine (to form quinone) in PGA-DA&T4 hydrogel was confirmed by the appearance of a new peak at 1650 cm^{-1}, which corresponds to the stretching vibration of the C═N double bond (Fig. 1A). The successful incorporation of NH_2-T4-POSS segments into PGA-T4 was further confirmed by the show up of new peaks at 3.17, 1.48, and 0.46 ppm (peaks d', e', and f') in the ^{1}H NMR of PGA-T4 (Fig. 1B and S1B). Additionally, the X-ray diffraction (XRD) patterns in Fig. 1C demonstrate the characteristic peaks (26.9° and 45.4°) of dopamine in PGA-DA and peaks of NH_2-T4-POSS (59.1°, 66.5°, and 74.3°) in PGA-T4 respectively, confirmed the successful anchoring of these functional monomers on PGA. These peaks were also detected in the XRD spectra and a new peak (40.8°) appeared in the XRD pattern of PGA-DA&T4 hydrogel, implying that the composite of the two precursors influences the PGA molecular structure.

Thermal stability significantly affects material performance. Fig. 1D presents the typical DSC profiles of γ-PGA and modified PGAs obtained via second heating sequences (25–275 °C). The modified PGAs showed a sharp rightward shift of the exothermic peak and lower exothermic enthalpy compared to γ-PGA, indicating enhanced thermal stability of the functionalized PGA polymers. The PGA-DA&T4 exhibited a significant increase in melting point, indicating strong chemical cross-linking. The thermal degradation curves of both γ-PGA and the functional PGAs, ranging from 30 to 650 °C, are shown in Fig. 1E. The TGA data shows that the T^d_{max} (the maximum of thermal degradation temperature) of the functional PGAs all close to 320 °C, significantly higher than that of γ-PGA (240 °C). The ultimate char yield of PGA-DA&T4 hydrogel was near two times higher than the unmodified γ-PGA (top right of Fig. 1E). The above results demonstrate the excellent thermal stability of modified PGA, especially PGA-T4 and PGA-DA&T4, comparing unmodified γ-PGA, which is beneficial for bone regeneration applications.

The morphology and three-dimensional porous architecture of the freeze-dried hydrogels were observed by field-emission scanning electron microscope (FE-SEM) (Fig. 1F). As illustrated from the SEM images, all hydrogels presented good interpenetrating macroporous structures, but obvious differences in the size dimension of fibers between γ-PGA and the modified PGAs. Compared to the others, the surface and interior

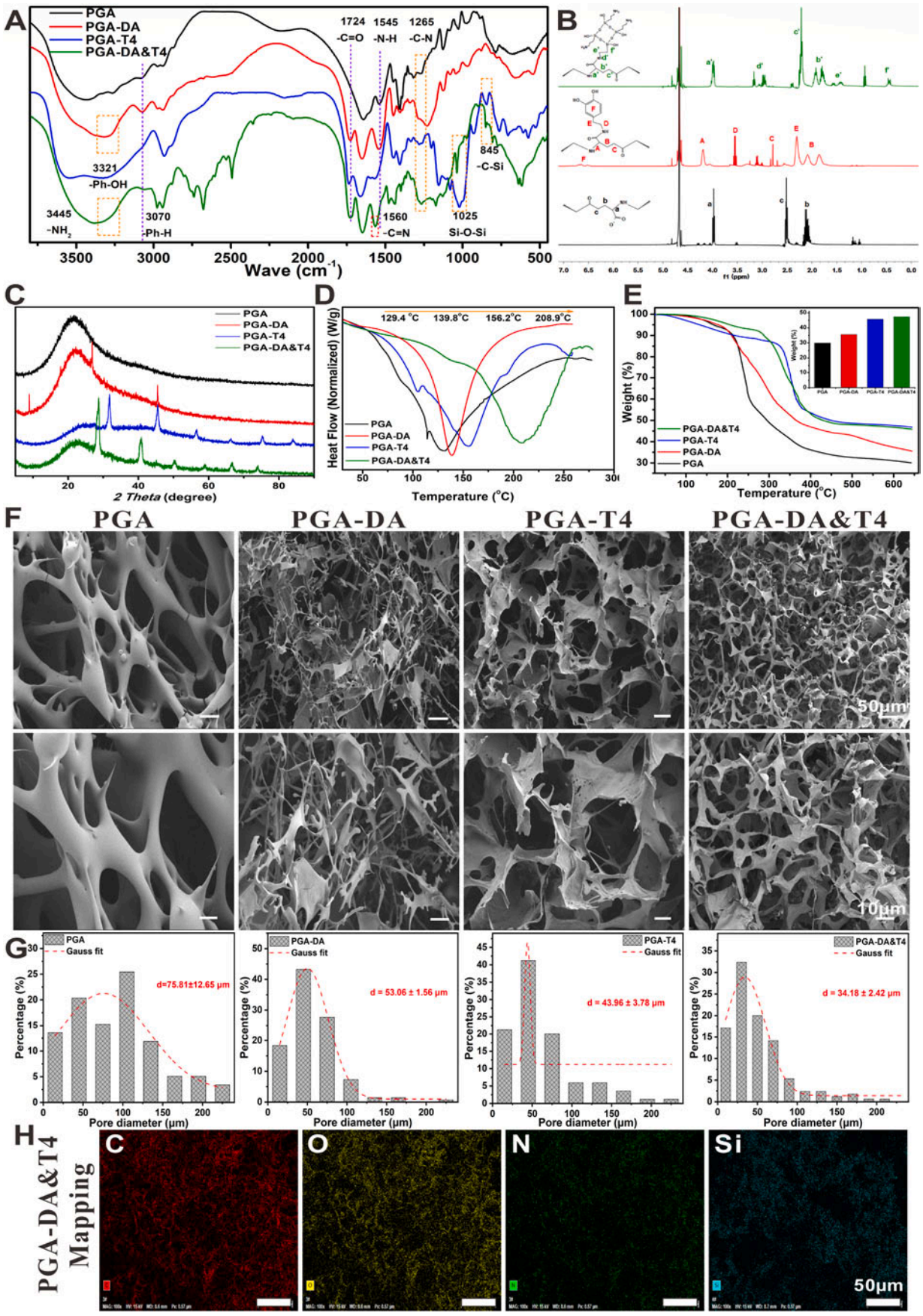

Fig. 1. Characterization of the hybrid PGA hydrogels. A) FT-IR, B) ^{1}H NMR, C) XRD patterns, D) DSC, and E) TGA results of PGA and hybrid PGA hydrogels, respectively; F) SEM images, G) pore size distribution, and H) SEM-EDS elemental mapping of PGA, PGA-DA, PGA-T4, and PGA-DA&T4 hydrogels, respectively.

of PGA-DA&T4 composite hydrogel were relatively ordered and exhibited a more compact hydrogel with a smaller size and more homogeneous distributed porous structure (Fig. 1F). As shown in Fig. 1G, the average pore size of PGA-DA&T4 decreased to 34.18 ± 2.42 μm compared with those of PGA-T4 (43.96 ± 3.76 μm), PGA-DA (53.06 ± 1.56 μm), and PGA (75.81 ± 12.65 μm). Moreover, the pore arrangement and 3D micro-fold structure of the PGA-DA&T4 hydrogel were tightly ordered since more bonds formed partially incorporated crosslinking in the hydrogel. The good consistency between the macropore size of hydrogel and the bone chamber is not only conducive to cell migration and adhesion but also can promote the penetration, growth, and osteogenic differentiation of stem cells.

Additionally, from PGA, PGA-DA, PGA-T4 to PGA-DA&T4, the porosity of the composite hydrogels increased (Fig. S2A), and the swelling ratios also improved (Fig. S2B). The interpenetrated 3D porous architecture can effectively facilitate cell migration and induce directed enrichment, which contributes to the excellent bone regeneration. Besides, typical energy-dispersive X-ray spectroscopic (EDS) profiles for the surface of PGA-DA&T4 and the associated elemental mapping for C, O, N, and Si atoms shown in Fig. 1H indicate the uniform distribution of grafted NH_2-T4-POSS. The EDS elemental maping results of the other three groups are presented in Fig. S3A, B, and C, effectively.

Interestingly, PGA-T4 and PGA-DA&T4 exhibited self-polymerizable and self-healing ability. As shown in Fig. 2A, without adding any crosslinker or crosslinking initiator, PGA-T4 solution could self-crosslinked into hydrogel, the gel time was around 100 min at 25 °C. In contrast to the slow self-crosslinking of PGA-T4, the introduction of PGA-DA making the hybrid PGA-DA&T4 solution rapidly crosslinked into stable hydrogel within 5 min. The viscosity testing results of different hydrogels are shown in Fig. 2B, the viscosity of PGA-DA&T4 was significantly higher than others under the frequency within the range of 0.1–200 Hz. Clearly, preferable injectability and viscoelasticity of the hybrid hydrogel were testified under the continuous control frequencies, manifesting that the hybridization of multiple bonds could improve the viscoelasticity of hydrogel, agreeing on the highest viscosity possessed by PGA-DA&T4. The prepared hydrogels' injectability was also confirmed by typing alphabets using a syringe filled with PGA-DA&T4 hydrogel. The favorable shape adaptibity of the hydrogels is helpful to fulfill the complex bone defects for bone regeneration applications (inner graph in Fig. 2B).

A strain sweep measuring the energy storage modulus (G′) and loss modulus (G″) was conducted to investigate the rheological performence of composite hydrogels. As presented in Fig. 2C and D, for PGA and PGA-DA, the G″ values were all higher than the G′ values in the whole testing range from 0.1 to 100 rad/s, indicating that no stable hydrogels were formed for PGA and PGA-DA solutions, While, for both PGA-T4 and PGA-DA&T4, the values of G′ were consistently higher than G″, indicating that the two hydrogels were stable and possessed an excellent three-dimensional structure with desirable elasticity. Morover, the PGA-DA&T4 composite hydrogel showed higher G′ and G″ values than others with the increase of frequency, suggesting that a rapid gelation of PGA-DA&T4 hydrogel occurred via host-guest hybrid complexation which drove supramolecular assembly to form a more robust crosslinking bond. The G′ and G″ change trend of both PGA-T4 and PGA-DA&T4 hydrogels in the range of 0.01 %–500 % strain amplitude are shown in Fig. S4. Moreover, PGA-T4 and PGA-DA&T4 hydrogels exhibited favorable self-healing ability (Fig. S5), which is also confirmed by that after relaxation (10 % strain) for 200s following 200s of subjection to a large strain (3000 %), the G′ of PGA-T4 and PGA-DA&T4 (especially for the later one) could be mostly restored even after 2 cycles (Fig. 2E and F). At low strain (10 %), PGA-DA&T4 possessed nearly doubled G′ value (~1200 Pa) comparing that of PGA-T4 (~600 Pa), further confirming that denser and stronger reversible cross-linkages were formed in PGA-DA&T4 hydrogel (Fig. 2F). While, for PGA, the G′ values were all lower than the G″ values either at low (10 %) or large (3000 %) strain, and for PGA-DA, once more confirming that no gelation occurred for PGA during the whole testing process (Fig. S6A). For PGA-DA, although the G′ values were higher than the G″ values at low strain (10 %), the difference between G′ and G″ became much smaller at the third cycle, proving that PGA-DA hydrogel was not stable (Fig. S6B).

For successful bone regeneration, appropriate mechanical properties are vital characteristics enabling hydrogels to withstand the physiological strain of bone tissue, and good adhesion property also plays an important role in osteointegration. As shown in Fig. S7, PGA-T4 and PGA-DA&T4 hydrogels demonstrated ubiquitous adhesion against glass and plastic surfaces even after shearing and self-healing. The adhesion strengths of PGA and modified PGAs against procine skin were also quantitatively measured. As shown in Fig. 2G and H, the adhesion strength of PGA-DA (52.79 ± 3.66 kPa) and PGA-T4 (42.68 ± 4.18 kPa) against porcine skin were all higher than that of PGA (34.51 ± 2.37 kPa), with PGA-DA&T4 (63.0 ± 3.41 kPa) showing the highest adhesion strength in all the tested samples. The strong tissue adhesion strength of PGA-DA&T4 is believed to be derived not only from mussel-inspired chemical bonding between the catechol groups and the nucleophilic groups (-NH_2, –COOH, –OH) on tissue surface [33,35–38], but also from the cohesion strength enhancement by the introduction of T4 in the hybrid PGA-DA&T4 hydrogel.

Comparing with PGA (0.56 ± 0.02 MPa) and PGA-DA (1.05 ± 0.03 MPa), the tensile strengths of PGA-T4 (2.38 ± 0.03 MPa) and PGA-DA&T4 (2.67 ± 0.04 MPa) were significantly higher, proving the cohesion enhancement performance of the introduction of T4 (Fig. 2I and J). As shown in Fig. 2J, the Young's moduli of PGA-T4 (4.82 MPa) and PGA-DA&T4 (3.73 MPa) were significantly higher than PGA(1.45 MPa) and PGA-DA (1.93 MPa), indicating that the introduction of T4 and the composition of PGA-DA and PGA-T4 polymer chains in PGA-DA&T4 hybrid hydrogel significantly improved the rigidity and enhanced crosslinking density. Denser chemical/hydrogen bonding crosslinking and much tighter polymer chain entanglements were formed between the polymer chain segments in PGA-DA&T4 hybrid hydrogel, which not only improved the cohesion energy and structure stability, but also promoted tissue adhesion strength. Furthermore, different from normal polymer films that the elongation always decreases along with the increase of Young's modulus, the elongation at break of PGA-DA&T4 (220.4 ± 6.4 %) was also the biggest in all tested samples (Fig. 2I). This might be sttributed to the aboundance of hydrogen bonding interaction and the self-healing ability of PGA-DA&T4 hydrogel. Moreover, the stress-strain curves and elastic moduli for the PGA-T4 and PGA-DA&T4 hydrogels after shearing and self-healing are demonstrated in Fig. S8, the Young's modulus and elongation at break of PGA-DA&T4 hydrogel were still maintained at 3.27 MPa and 182.60 %. These results demonstrate that the formation of Schiff-base bonding within the PGA-DA&T4 hydrogel, as well as the further stabilization of the hydrogel structure upon the condensation of Si–OH with catechol groups, can significantly enhance the mechanical strengths and self-healing ability of the hybrid hydrogels. The high elasticity and favorable adhesive properties of the modified PGA hydrogels are benefical for their bone regeneration applications.

To simulate *in vivo* biodegradation property, an *in vitro* degradation study of PGA and the modified PGA hydrogels were conducted in PBS (pH ~7.4) at 37 °C. As presented in Fig. 2K, the degradation rates of the modified PGA hydrogels from 0 to 14 weeks, were visibly lower than that of the pure PGA film, reflecting the enhancement of internal crosslinking in the modified hydrogels. The degradation of PGA-DA&T4 hydrogel (30.5 ± 2.35 % on day 70 vs. 3.9 ± 1.02 % on day 28) were significantly slower than PGA film (80.9 ± 3.08 % on day 70 vs 30.1 ± 1.22 % on day 28). After 98 days' degradation, a weight percentage of 57.3 ± 2.13 % for PGA-DA&T4 hydrogel was still undegradaed (Fig. 2K). Longer degradation time might be beneficial for bone regeneration to maintain essential mechanical stability before newly formed bone fullfil the bone defect cavity. Besides, the release behavior of dopamine and NH_2-POSS-T4 NPs from either PGA-DA, PGA-T4 and PGA-DA&T4 hydrogels was also investigated. As shown in Fig. 2L, the

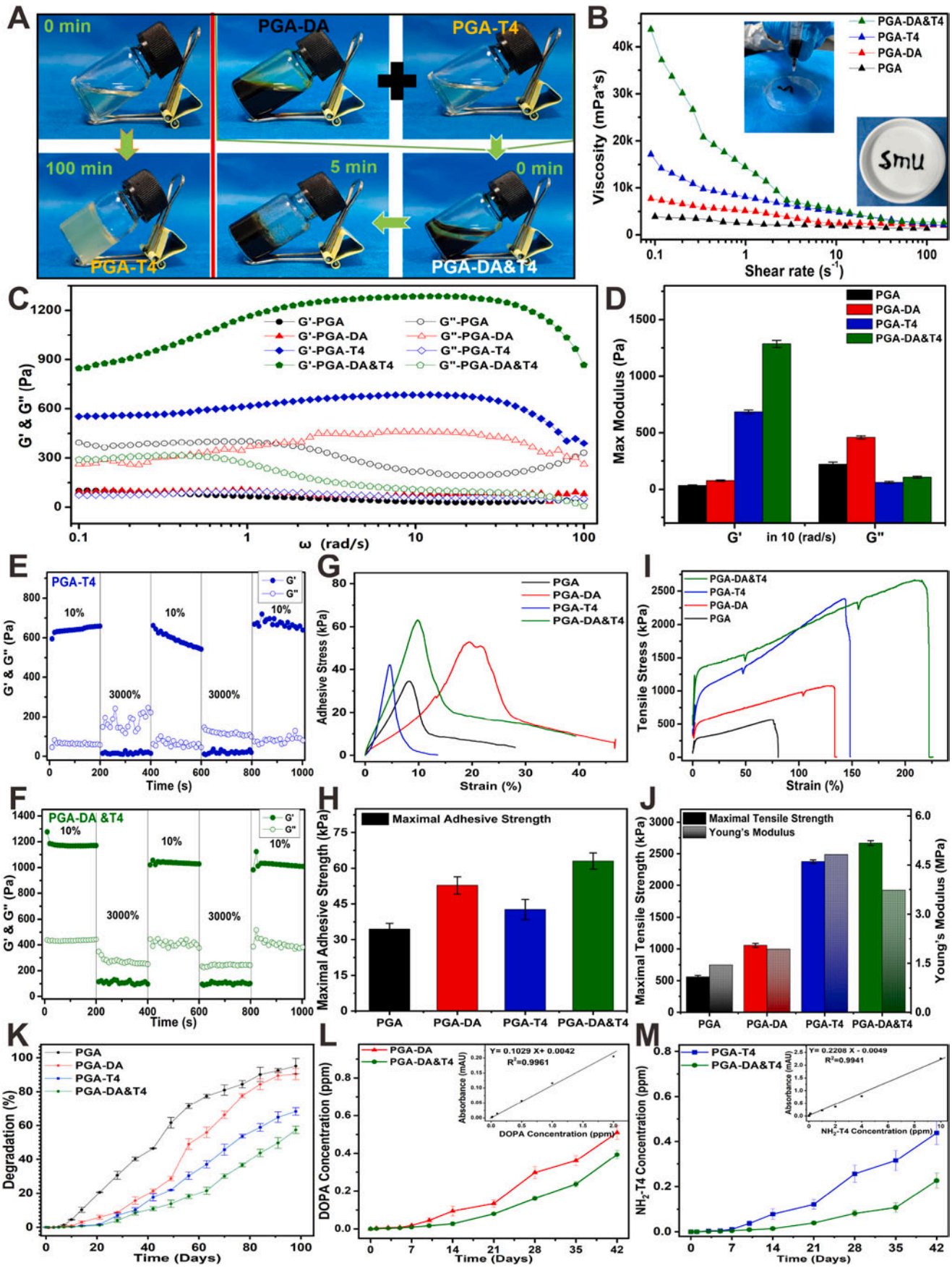

(caption on next page)

Fig. 2. Physicochemical behaviors and self-healing properties of PGA and hybrid PGA hydrogels. A) Gelling time and appearance of prepared hybrid PGA hydrogels before and after gelation. B) Rheological behaviors of hybrid hydrogels at 37 °C, and photos of injectable objects (PGA-DA&T4 as an example). C) Viscoelastic properties and D) modulus under 10 rad/s of different hydrogels. The cyclic step-strain measurements of E) PGA-T4 and F) PGA-DA&T4 hydrogels demonstrate the shear-yielding behavior and corresponding self-healing under repeated experiments at 37 °C, respectively. G) Adhesive capacity curves and H) maximum adhesion strength of composite hydrogels adhering to fresh pigskin. I) Tensile stress–strain curves and J) Young's modulus for the different hydrogels. K) The *in vitro* degradation curves of the PGA and modified PGA hydrogels. The release behaviors of L) catechol active moiety (determined by dopamine) and M) NH_2-POSS-T4 NPs from the PGA-DA, PGA-T4, and PGA-DA&T4 hydrogels, respectively. Data are presented as mean values ± SD (n = 3).

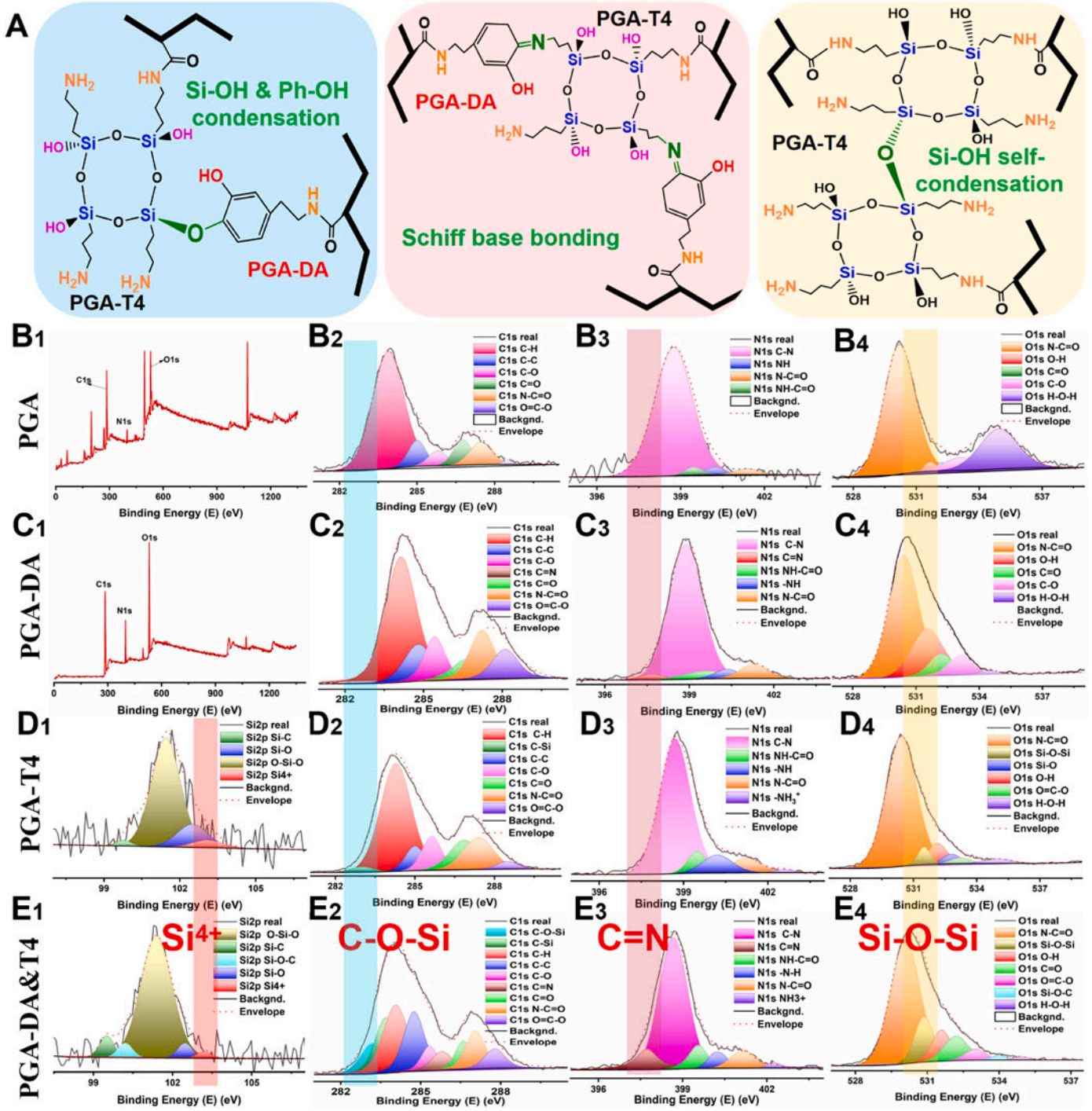

Fig. 3. Characterization of the crosslinking mechanism of hybrid hydrogels. A) Schematic diagram of PGA-DA&T4 hydrogel cross-linking reaction for the hybrid synthesis. B-E) X-ray photoelectron spectroscopy (XPS) analysis to investigate the surface chemical composition of various hydrogels with PGA, PGA-DA, PGA-T4, and PGA-DA&T4, respectively.

release of catechol group (determined by dopamine), as anti-reactive oxygen species (ROS) active moiety, from PGA-DA&T4 hybrid hydrogel was much slower and more durable when compared with PGA-DA modified by dopamine alone. The active NH_2-T4-POSS release behavior from PGA-DA&T4 hybrid hydrogel was similar with catechol components from PGA-DA&T4 (Fig. 2M), which might be beneficial to effectively regulate the bone regeneration immune microenvironment. Furthermore, our analysis revealed that the release rate of both catechol components and NH_2-T4-POSS from PGA-DA&T4 was slower compared to their release rate in the DA or T4 solely modified PGA hydrogels. This can be attributed to the formation of robust reversible Schiff-base bonds between catechol groups and amine groups homogeneously distributed in the PGA-DA&T4 network. The porous structure of the hybrid hydrogels also facilitates substance delivery (Fig. 1F). As an important component of the polymer chain of PGA, the release rate of L-glutamate decreased significantly after DA, T4 or DA&T4 modifications, while the two-phase hybrid PGA-DA&T4 hydrogel exhibited the slowest L-glutamate release (Fig. S9).

2.2. Mechanism of PGA-DA&T4 multidimensional self-polymerization reinforcement

To understand the mechanical property improvement mechnism of the PGA-DA&T4 hybrid hydrogel, the multi-scaled structure of the modified hydrogels and the molecular interactions between active ingredients (catechol and NH_2-T4-POSS) and PGA polymer chains were investigated. Fig. 3A shows the bonding reaction in multidimensional self-polymerization of the three main strongly interacting molecular structures of hybrid PGA-DA&T4 hydrogel to form robust cross-linkage. The possible strong cross-linkages include reversible condensation of the Si–OH groups with the Ph-OH groups (from dopamine), Schiff-base bonding, and self-condensation of Si–OH groups. To investigate the surface chemical composition and bonding states of the different hydrogels, X-ray photoelectron spectroscopy (XPS) analysis was employed to verify the interaction mechanisms of multiple cross-linking bonds (Fig. 3B–E). Table S3.1-3.4 further summarizes the proportion of C, N, O, and Si elements in all hydrogels for comparison.

Fig. 3B_1, C_1, and S10A-10B show the wide survey spectrums of PGA, PGA-DA, PGA-T4, and PGA-DA&T4 samples, which indicate the presence of C, O, and N atoms. Additionally, Si atoms were able to be detected in PGA-T4 and PGA-DA&T4 hydrogels. The XPS C1s emission of all prepared samples can be Gaussian simulated into six-component peaks, vesting in the C–H (284.2 eV), C–C (284.8 eV), C–O (285.4 eV), C═O (286.6 eV), O═C–N (287.2 eV) and O═C–O (287.8 eV), respectively (Fig. 3B_2, 3C_2) [39,40]. The C–N peaks were derived from PGA-DA and the C═N peak was from the self-polymerization of dopamine. The high-resolution C1s spectra of PGA-T4 and PGA-DA&T4 are shown in Fig. 3D_2 and 3E_2, respectively. These spectra can also be fitted into C–Si (283.8 eV) in addition to the above peaks, demonstrating the successful introduction of NH_2-T4-POSS into the PGA polymer. The successful cross-linking reaction between the Si–OH groups with the Ph–OH groups was proved by the show up of a new peak of C–O–Si (283.4 eV) in the C1s emission of PGA-DA&T4 (Fig. 3E_2 and the left panel of Fig. 3A). In addition, the C═N (285.9 eV) peaks were also detected in PGA-DA&T4 and the relative area (7.06 %) is significantly higher than that in PGA-DA (0.65 %Ta ble S3.1), which was from the polymerization between the dopamine and free amine groups on NH_2-T4-POSS, indicting a sufficient formation of Schiff-base bonds in hybrid PGA-DA&T4 hydrogel (the middle panel of Fig. 3A).

Fig. 3B_3-3E_3 show the Gaussian curve-fitting peak of N1s for PGA, PGA-DA, PGA-T4 and PGA-DA&T4. Compared with the N1s peaks of pure PGA, a stronger signal of N1s peak was observed (Fig. 3C_1), a new peak of Schiff-base C═N (397.7 eV) presented in PGA-DA and the relative area of –NH (400.2 eV) peak was also increased from 2.70 % for PGA to 4.18 % for PGA-DA (Fig. 3B_3 & 3C_3 and Tab le S3.1), which might be attribute to new amide group formation by the carboxyl groups on PGA and amino groups from dopamine [41]. Specifically, the $-NH_3^+$ peak at 402.2 eV was observed for PGA-T4 and PGA-DA&T4, indicating that NH_2-T4-POSS was successfully introduced onto the PGA chain and the formation of Schiff-base bonding in PGA-DA&T4 (Fig. 3D_3 & 3E_3 and Table S3.2). The formation of Schiff-base bonding in PGA-DA&T4 was also confirmed by the increase of the relative area of C═N peak under N1s envelop increased from 1.23 % for PGA-DA to 11.7 % for PGA-DA&T4.

Moreover, the high-resolution narrow scans of O1s core-level spectra of the PGA and modified PGA samples are displayed in Fig. 3B_4-3E_4 for comparasion. The O1s emission were devided into five typical peaks (O═C–N, O–H, C═O, C–O, and H–O–H) in PGA, while the new peak of Si–O–Si (531.0 eV) appeared in PGA-T4 and PGA-DA&T4 (Fig. 3D_4 & 3E_4), further verifying the effective bonding reaction between NH_2-T4-POSS and PGA matrix according to previous analysis. Combined with the increase of the relative area of –OH peak (531.7 eV) and decreased relative area of C═O peak (532.2 eV) under O1s envelop (Fig. 3C_4 & E_4 and Ta ble S3.3), it can be concluded that the oxidized quinone groups in PGA-DA interacted with amino groups in PGA-T4 (the middle panel of Fig. 3A). However, the generation of new peaks Si–O–C (533. eV) in PGA-DA&T4 and the relative area of Si–O–Si peak increased from 3.94 % for PGA-T4 to 4.21 % for PGA-DA&T4 (Fig. 3D_4 & 3E_4), indicating that the self-condensation of Si–OH groups in PGA-T4 and polymerization with phenolic hydroxyl in PGA-DA occurred to construct multiple effective cross-linking bonds (Fig. 3A). These results support the high structure stability, robust mechanical properties, and relatively weak biodegradable ability of the hybrid PGA-DA&T4 hydrogel.

As shown in Fig. 3D_1 and 3E_1, the deconvolution of Si2p spectra of the PGA-T4 containe four characteristic peaks near 99.5, 100.2, 101.4, and 102.4 eV, assign to Si–O–Si, Si–C, Si–O, and Si^{4+} ions, respectively [42–44]. Similar to the emission of O1s, a new peak of Si–O–C (103.2 eV) was observed in PGA-DA&T4. Additionally, the relative area of the Si–O–Si peak (99.5 eV) increased from 4.40 % for PGA-T4 to 5.95 % for PGA-DA&T4 (Fig. 3E_1 and T able S3.4). This suggests that multiple bonding cross-linkages occurred through the interaction of Si–OH groups with the Ph-OH groups in PGA-DA&T4. Meanwhile, the Si^{4+} ions peak was observed obviously around 102.4 eV in the Si2p spectrum of PGA-T4 and PGA-DA&T4 hydrogels, indicating the formation of the silicate-like structure in the two groups, which could promote angiogenesis and regulate osteogenic differentiation. As the relative peak area of Si^{4+} ions increased from 8.78 % for PGA-T4 to 14.29 % for PGA-DA&T4 (T able S3.4), it is believed that the introduction of dopamine might promote more thorough hydrolysis of NH_2-T4-POSS and endow better ROS scavenging ability, beneficial for regulating the induction of bone regeneration micro-environment towards osteogenesis. Overall, the results of curve-fitting for C, N, O, and Si elements in XPS spectra, along with the presence of typical bonds of PGA, dopamine, NH_2-T4-POSS, and new cross-linking interactions in the PGA-DA&T4 group, demonstrate the successful fabrication of the hybrid multidimensional self-polymerizable hydrogels as designed. These results are in agreement with the conclusions derived from FT-IR and XRD analyses.

2.3. Cytocompatibility and bioactivity of the modified PGAs

The hydrogels' cytocompatibility was evaluated using BMSCs via CCK-8 assay and Live/Dead staining kit. Firstly, we use different concentrations of material degradation products to screen for the optimal concentration for subsequent cell experiments. Fig. 4A shows that the material exhibits significant toxicity at 1000 μg/mL (below 40 %), but there is no difference compared to the control group at 100, 50, and 20 μg/mL, indicating that the hydrogel did not have a toxic effect on the cells. Based on the experimental results, subsequent cell experiments were conducted using a material concentration of 100 μg/mL. As shown in Fig. 4B and C, the control, PGA, PGA-DA, PGA-T4, and PGA-DA&T4 groups exhibited favorable cell morphology and proliferation status under dead-live staining. This confirms the hydrogel system's excellent

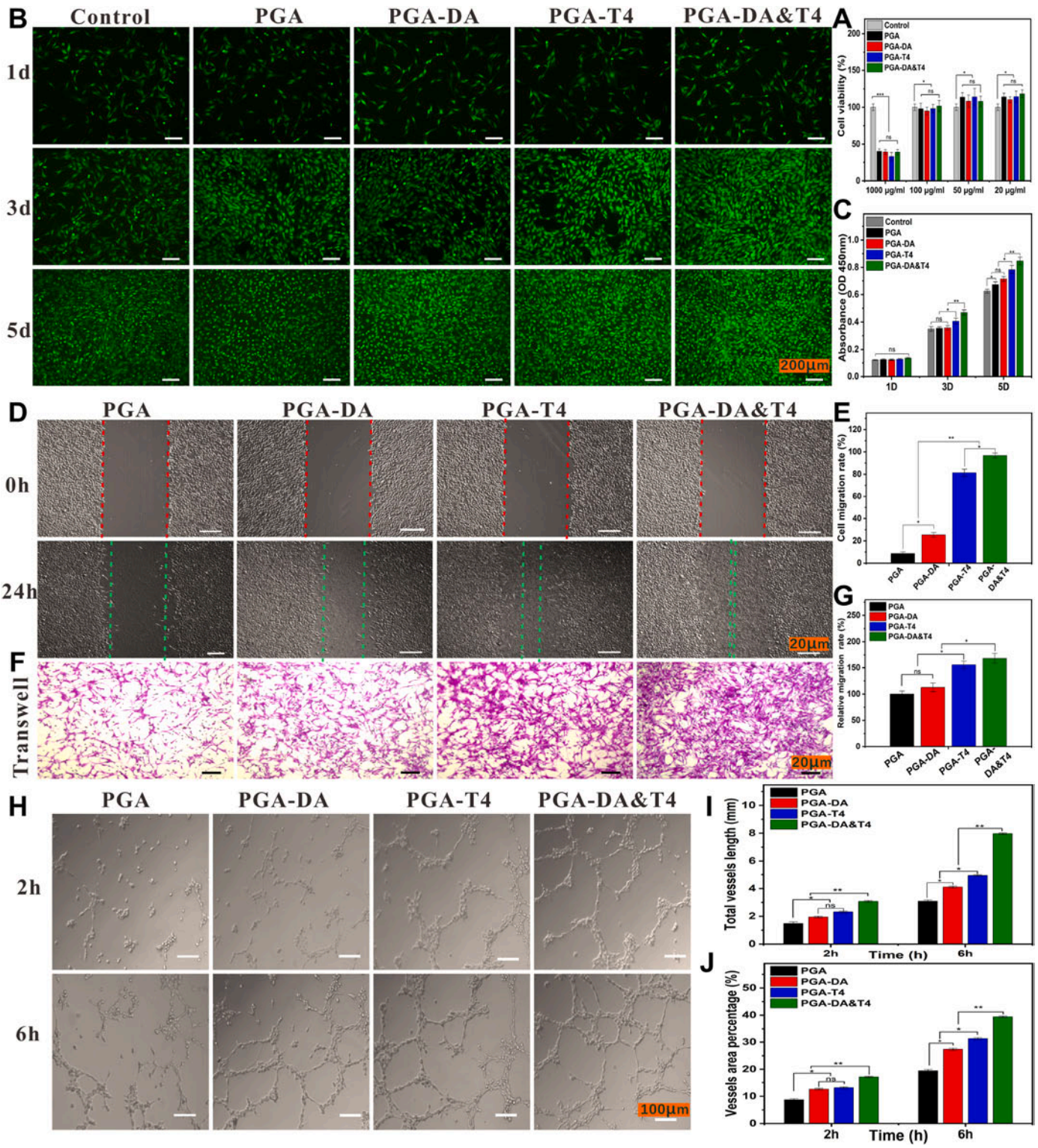

Fig. 4. Cytocompatibility and biological activity of PGA and modified PGA hydrogels. A) Cell viabilities of BMSCs co-cultured with different amounts of hydrogels. B) Representative Live/Dead staining images and C) quantitative OD values of co-cultured BMSCs after 1, 3, and 5 days. D) Scratch assay and E) corresponding cell migration rates; F) transwell migration assay and G) the corresponding relative migration rates of HUVECs co-cultured with the 10 × degradation products of PGA hydrogels. H) Representative microscopy images, the I) vessel area percentages and J) total vessel lengths of different groups by co-cultured HUVECs with the 10 × degradation products of PGA hydrogels for 2 and 6 h. Data are presented as mean ± SD (n = 3), ("ns" represents no significant difference, *$p < 0.05$, **$p < 0.01$, and ***$p < 0.001$).

biocompatibility and supports its potential *in vivo* application.

Furthermore, the effect of unmodified/modified PGAs to the migration ability of BMSCs was evaluated using cell scratch and transwell assays. As shown in Fig. 4D and E, after 24 h, the cell migration rates of the PGA-T4 (~82 %) and PGA-DA&T4 (~96 %) groups were significantly higher than that of the PGA-DA (~28 %), and the PGA (~9.5 %) groups, indicating the strong cell migration promotion ability of introducing T4 in PGA. This is further confirmed by the transwell (longitudinal migration) assay results shown in Fig. 4F and G, in which the relative cell migration rates of PGA-T4 (~165 %) and PGA-DA&T4 (~175 %) were also significantly higher than that of PGA-DA (~115 %) and PGA (set as 100 %). The favorable cell migration promotion ability PGA-DA&T4 is deemed to be derived from the introduction of both DA and NH_2-T4-POSS (T4), especially the later. The cell migration promotion ability of PGA-DA&T4 is beneficial to promote stem cell migration, creating an environment to support the recruitment of related cells,

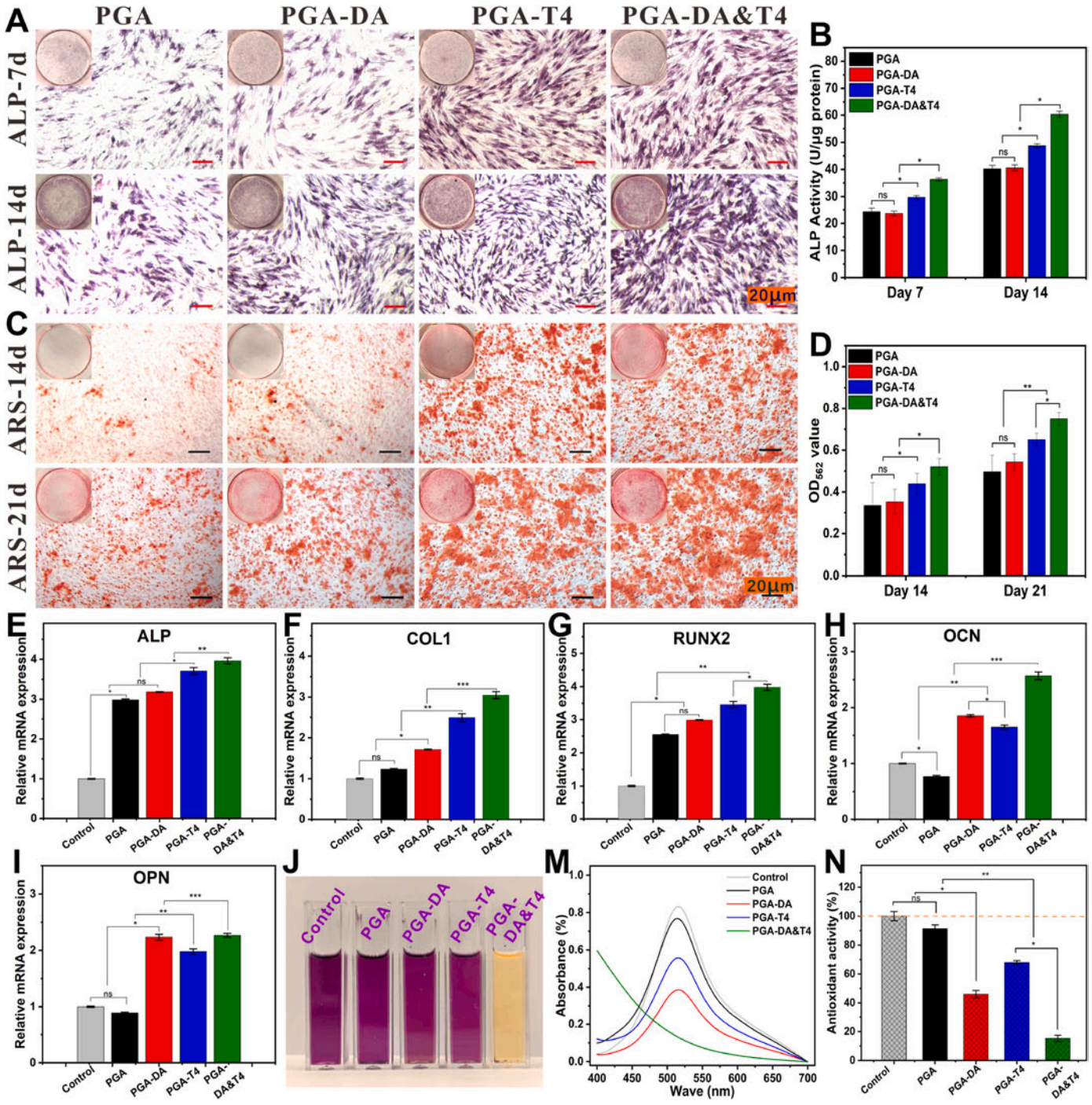

Fig. 5. The osteogenic properties and antioxidant activity of PGA hydrogels. A) Alkaline phosphatase (ALP) staining images and B) quantitative ALP activities of osteogenic differentiated BMSCs on day 7 and 14; C) Alizarin red S straining images and D) quantitative analysis results on day 14 and 21 after co-culturing with PGA and modified PGA hydrogels. *E*-I) The mRNA expression levels of osteogenic-related proteins including ALP, COL1, Runx2, OCN, and OPN evaluated by qPCR. J) Antioxidant color changing figures, M) UV–vis spectra, and N) DPPH radical scavenging activity of PGA and modified PGA hydrogels. Data are displayed as mean values ± SD (n = 3). "ns" represents no significant difference, *$p < 0.05$, **$p < 0.01$, and ***$p < 0.001$. (For interpretation of the references to color in this figure legend, the reader is referred to the Web version of this article.)

leading to enhanced tissue regeneration and bone repair. These results suggest that the modified PGA hydrogels, especially PGA-T4 and PGA-DA&T4 hydrogels are cytocompatible and can promote cell proliferation and migration, making them suitable for bone defect healing.

It is critical to induce angiogenesis for bone regeneration especially for huge bone defect or in poor bone regeneration microenvironment such as osteoporosis. As shown in the results of the angiogenesis experiments (Fig. 4H), the PGA-T4 and PGA-DA&T4 groups (especially the later one) already induced some tubular structures as early as 2 h, at which time the PGA and PGA-DA groups showed nearly no formation of tubular structures. After 6 h, more tubular structures formed for samples other than PGA, and the PGA-DA&T4 group exhibited the most comprehensive angiogenesis with the densest and longest tubular network (Fig. 4H–J). It is believed that the PGA-T4 and PGA-DA&T4 hydrogels induced neovascularization is primarily through the promotion of endothelial cell proliferation and vascular sprouting by silica ions (Si^{4+}) [17,45], and the creation of a lower oxidative stress environment for angiogenesis by catechol groups. The PGA-T4 and PGA-DA&T4 hydrogels facilitate vascularization thus assist in the early trophic-functional reconstruction of tissues during bone defect healing.

2.4. Osteogenic properties of the modified PGAs

The effect of the modified PGAs to the osteogenic differentiation and bone mineralization of BMSCs as well as the secretion of osteogenic marker proteins was investigated via ALP and alizarin red (ARS) staining, ALP quantitative assay kit, and qPCR. It can be seen from Fig. 5A and B that the PGA-T4 and PGA-DA&T4 groups demonstrate a significant increase in ALP expression levels at both 7 and 14 days the initiation of osteogenic differentiation. Furthermore, T4 modification was found also significantly increased the mineralization of osteogenic differentiated BMSCs, as evidenced by the alizarin red staining images (Fig. 5C) and the quantitative ARS OD values at 662 nm (Fig. 5D), especially on day 21. Moreover, the gene expression levels of osteogenesis-related proteins, such as ALP, COL1, Runx2, OCN, and OPN, of the PGA-T4 and PGA-DA&T4 groups were also significantly higher than that of the control, PGA and PGA-DA groups (Fig. 5E–I). These results further confirm the promotional effect of dopamine grafting and T4 crosslinking of the hydrogel on osteogenesis.

2.5. Antioxidant capability, immunomodulation and osteoclast inhibition of the modified PGA hydrogels

The role of implant biomaterials in bone regeneration is affected by their antioxidant capacity. ROS can cause oxidative stress, amplify the inflammatory cycle, and disrupt osteogenic differentiation. To evaluate the antioxidant ability of PGA and modified PGA hydrogels, 2,2-diphenyl-1-picrylhydrazyl (DPPH) assay and intracellular ROS scavenging experiment were conducted. Intuitively, The modified PGA groups displayed much lighter color compared to the control and PGA groups, indicating an improvement in antioxidant capacity after modification (Fig. 5J). Fig. 5M–N shows that the absorbance of DPPH for PGA at 517 nm was similar to the control, exhibiting only a DPPH scavenging of ~7 %. However, the DPPH absorbances of the PGA-DA and PGA-T4 groups significantly decreased to ~43 % and 64 %, respectively. The PGA-DA's antioxidant capacity may be attributed to the successful grafting of dopamine, a typical mussel-inspired catechol moiety. While, the PGA-T4's may be due to the combination of $-NH^{3+}$ ions and the hydrolysis of silicon-oxygen bonds, as evidenced by the appearance of Si^{4+} ions (Fig. $3D_1$). The dual-network hybrid composite PGA-DA&T4 hydrogel showed significantly stronger DPPH scavenging ability (~90 %) compared to the two groups with single modification, as shown in Fig. 5M–N. We speculate that the superior anti-oxidant ability of PGA-DA&T4 comparing to PGA-DA may be attributed to the existing Schiff-base, which promotes the binding of $-NH^{3+}$ ions and the hydrolysis of silicon hydroxyl group with oxygen radicals. Furthermore, the intracellular ROS scavenging experiment was conducted by stimulating BMSCs to produce excess intracellular ROS using H_2O_2 and co-culture the cells with the hydrogels. The ROS probe, DCFH-DA which could be hydrolyzed to DCFH by esterase after entering the cell, and when DCFH encounters ROS, it turns into DCF and emits strong green fluorescence.

As demonstrated in Fig. 6A and **E**, the DCFH fluorescence intensity of cells treated with PGA-DA&T4 was significantly lower than that of the PGA-T4 group and the H_2O_2 group. Meanwhile, it was found that the PGA-T4 group also demonstrated considerable ROS scavenging ability. It deemed that dopamine modification confers strong antioxidant capability, and the introduction of T4 further enhances this effect; the antioxidant property may originate from the inorganic silica-oxygen backbone structure. These results confirm the favorable ROS scavenging efficacy of hybrid PGA-DA&T4 hydrogels, which could not only reduce the amount of endogenous ROS but also can effectively inhibit the production of ROS, conducive to providing a suitable immune microenvironment for bone regeneration.

The immunomodulatory capability of the modified PGAs was assessed by investigating the effect of the modified PGA hydrogels on macrophage polarization processes using Raw264.7 as the cell model. Exposure to lipopolysaccharide (LPS) induces the M1 phenotype, while exposure to interleukin-4 (IL-4) induces the M2 phenotype. In these experiments, cells exposed solely to LPS served as a negative control, while cells exposed solely to IL-4 served as a positive control. The remaining groups were treated with the material after exposure to LPS/IL-4. The promotion of macrophage polarization by the modified PGA hydrogels at the cellular level was initially assessed through immunofluorescence staining. As illustrated in Fig. 6B, macrophages treated with PGA-DA&T4 exhibited higher fluorescence intensity of CD206 protein compared to the other groups. The semi-quantitative results of immunofluorescence (Fig. 6F-6G) indicate that PGA-DA&T4 hydrogel decreased the percentage of LPS-induced CD86 fluorescence from 67 % to 24 % and increased the percentage of IL-4-induced CD206 fluorescence from 30 % to 74 %. These experimental results confirmed that the PGA-DA&T4 hydrogel effectively promoted the polarization of macrophages from the M1 phenotype to the M2 phenotype. This, in turn, improved the inflammatory microenvironment during bone repair and created favorable conditions for the osteogenic differentiation of bone marrow mesenchymal stem cells into osteoblasts.

The tissue microenvironment also affects osteoclastogenesis during bone formation. On the third day of differentiation from mononuclear giant cells to osteoblasts, PGA, PGA-T4, and PGA-DA&T4 were added to the culture system to observe their effects on osteoblasts. Fig. 6C shows that the T4 containing hydrogel groups (PGA-T4 and PGA-DA&T4) significantly inhibited osteoblast differentiation, with PGA-DA&T4 demonstrating the strongest inhibitory effect. The statistics for the osteoclast area also confirmed this phenomenon (Fig. 6H). In addition to the differentiation and formation of osteoclasts in the osteoporotic state, the function of osteoclasts likewise determines the extent of bone resorption. Therefore, we verified the bone resorption function of osteoclasts using bone plates shown in Fig. 6D, and the PGA-DA&T4 group also maintained the best bone resorption inhibition effect, which can be verified with the osteoclast differentiation experiment (Fig. 6H). Based on the literature, it has been found that silicon ions can inhibit osteoclast differentiation [27,28]. Therefore, we hypothesize that the attenuated osteoclast differentiation of PGA-DA&T4 was due to the NH_2-T4-POSS moiety, while the introduction of dopamine reduced ROS in the microenvironment, thus synergistically enhanced the osteoclast inhibitory effect.

2.6. In vivo study

To further invesitigate the bone regeneration efficacy of the modified PGAs, an *in vivo* study using femoral condyle defect models on osteoporosis SD rats was conducted, followed by micro-CT analysis and

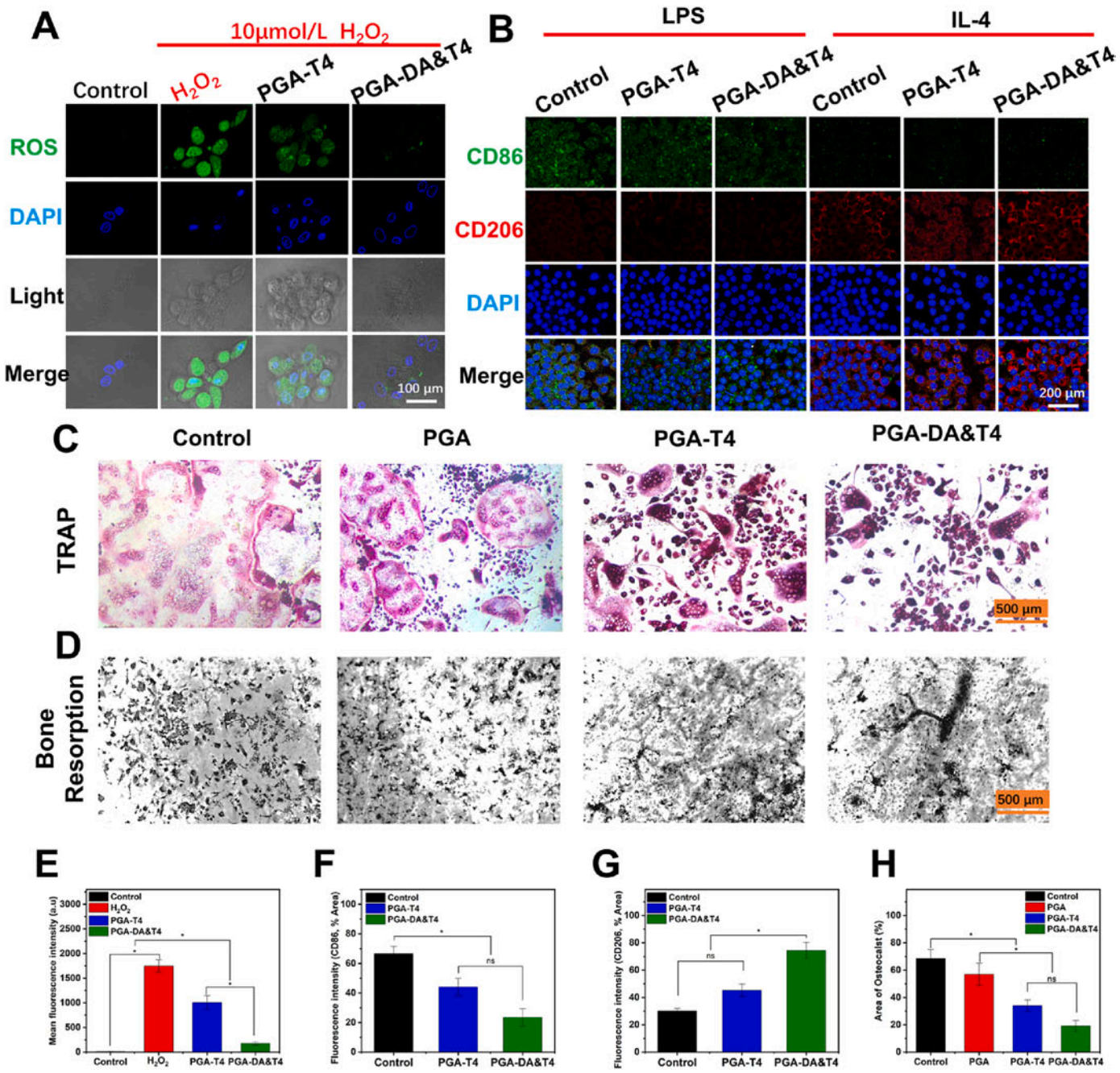

Fig. 6. Anti-oxidant activity and osteogenic regulatory functions of different PGA hydrogels. A) Intracellular H_2O_2 scavenging images using BMSCs and E) the quantitative analysis results. B) CLSM images of macrophages (RAW264.7) stained with CD86 antibody (green), CD206 antibody (red) and DAPI (blue) after treatment with LPS, IL-4 and hydrogels; C) Representative TRAP staining images of osteoclasts and D) photos of bone plate osteoclast bone resorption assay with different PGA hydrogels. Quantitative analysis of the relative protein levels of F) CD86 and G) CD206 protein. H) Areas of osteoblast calculated from the TRAP staining images. Data are presented as mean ± SD (n = 3) (scale bars are listed above; *p < 0.05, **p < 0.01, ***p < 0.005). (For interpretation of the references to color in this figure legend, the reader is referred to the Web version of this article.)

histological studies at 4 and 12 weeks after surgery. Fig. 7A (3D visualization and coronal section images) shows that the healing interface morphology of the PGA-DA&T4 group was superior to that of the other groups at both 4 and 12 weeks after surgery. At week 4, a complete bone cortical line was already visible in the PGA-DA&T4 group. At the 12th week after surgery, a significant amount of new bone was observed in the femoral condylar defect. As shown in the statistical analysis results of bone morphological parameters in Fig. 7B–D, the PGA-DA&T4 group demonstrated the highest bone mineral density, bone volume fraction, number of trabeculae, and trabecular thickness compared to the other groups. These results prelimilarly confirms the osteogenic ability of the PGA-DA&T4 *in vivo*, which is critical for bone defect healing. To observe the restored microstructure, we stained and analyzed the harvested tissues (see Fig. 7E). By week 4, we found that the bone defects in all groups had not completely healed, and immature granulation tissue containing a small amount of collagen was present in the area of the bone defects. The PGA-DA&T4 group had less inflammatory cell infiltration and more regular morphology and arrangement of the neoplastic tissue compared to the control and PGA groups. By week 12, the repair process was gradually completed. Additionally, the collagen fibers in the PGA-T4 and PGA-DA&T4 groups seemed denser than in the other groups. The PGA-DA&T4 group exhibited better osteogenesis and

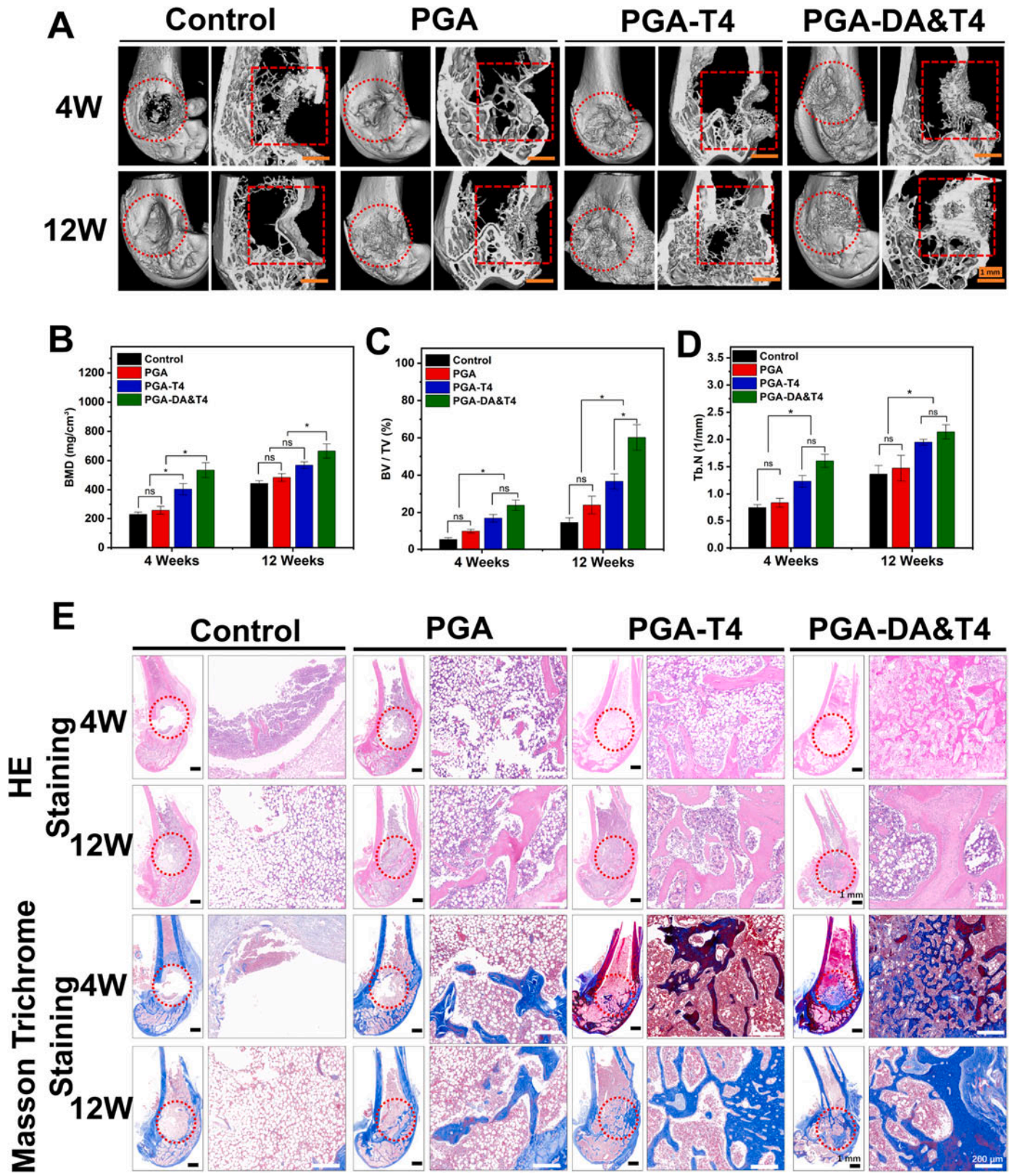

Fig. 7. Micro-CT and histological staining images. A) Typical micro-CT 3D reconstruction images of new bone regeneration in femoral condylar defect areas after 4 and 12 weeks. B-D) Quantitative indexes of micro-CT parameters in different treatment groups at 4 and 12 weeks: B) BMD, C) Bv/Tv, and D) Tb.N. E) H&E (top) and Masson's (bottom) staining images of the bone defect regeneration for different hydrogel treatments after 4 and 12 weeks. (Data are presented as mean ± SD (n = 3); scale bars 200um; *p < 0.05, **p < 0.01, ***p < 0.005).

superior histocompatibility during the bone regeneration process, which facilitated the reconstruction of bone defects.

Moreover, we observed the indicators of osteoblasts and osteoclasts through TRAP staining and OCN immunohistochemical staining. The TRAP staining and osteoclast quantification results are presented in Fig. 8A and D. The TRAP expression in the PGA-DA&T4 group and PGA-T4 group was significantly lower than that in the other groups at weeks 4 and 12. At week 12, different from that the number of osteoclasts in the control and PGA groups increased over time, the PGA-DA&T4 and PGA-T4 groups maintained similar osteoclast expression as at week 4. This suggests that the PGA-DA&T4 hydrogel not only inhibited osteoclasts but also maintained their biological functions for a long time. Fig. 8B and E shows the results of immunohistochemical staining and OCN quantification. The PGA-DA&T4 group exhibited stable high OCN expression at weeks 4 and 12, consistent with the qPCR results (Fig. 5H), confirming the trend of the osteoclast indicators. To further evaluate the hydrogel's anti-inflammatory properties, we selected IL-1β as a representative and assessed the inflammatory response using immunohistochemical staining and semi-quantitative analysis, as shown in Fig. 8C and F. There was no difference in the expression of IL-1β between the materials in each group at the two-time points of week 4 and week 8. This verifies that the modified means of PGA-DA&T4 would not cause tissue toxicity to the animals. Remarkably, the above results confirm that PGA-DA&T4 hydrogel has good bio-safety and can facilitate the healing of bone defects in osteoporotic rats by inhibiting osteoclastogenesis while enhancing the osteogenesis.

3. Conclusions

In summary, we have highlighted that the organic/inorganic hybrid method for constructing multidimensional self-polymerizable hybrid PGA-DA&T4 hydrogels, dual-modified by semi-caged NH_2-T4-POSS and dopamine, results in a multilayered interoperable topology, elastic mechanical behavior, superior mechanical supportability, and enhanced osteoblastic bioactivity. The hybrid PGA-DA&T4 hydrogels, designed as a multi-inductively biomimietic bone scaffold, with the ability to modulate the immune micro-environment for angiogenesis, osteogenic differentiation, and biomineralization, thus facilitating the healing of osteoporotic bone defects. Our study proposes a new design strategy that utilizes a multidimensional self-polymerization mechanism to create biomimetic PGA-based materials that are more effective, stable, and safe for treating osteoporotic bone defects. This approach has demonstrated significant clinical potential in the field of osteoporosis therapy.

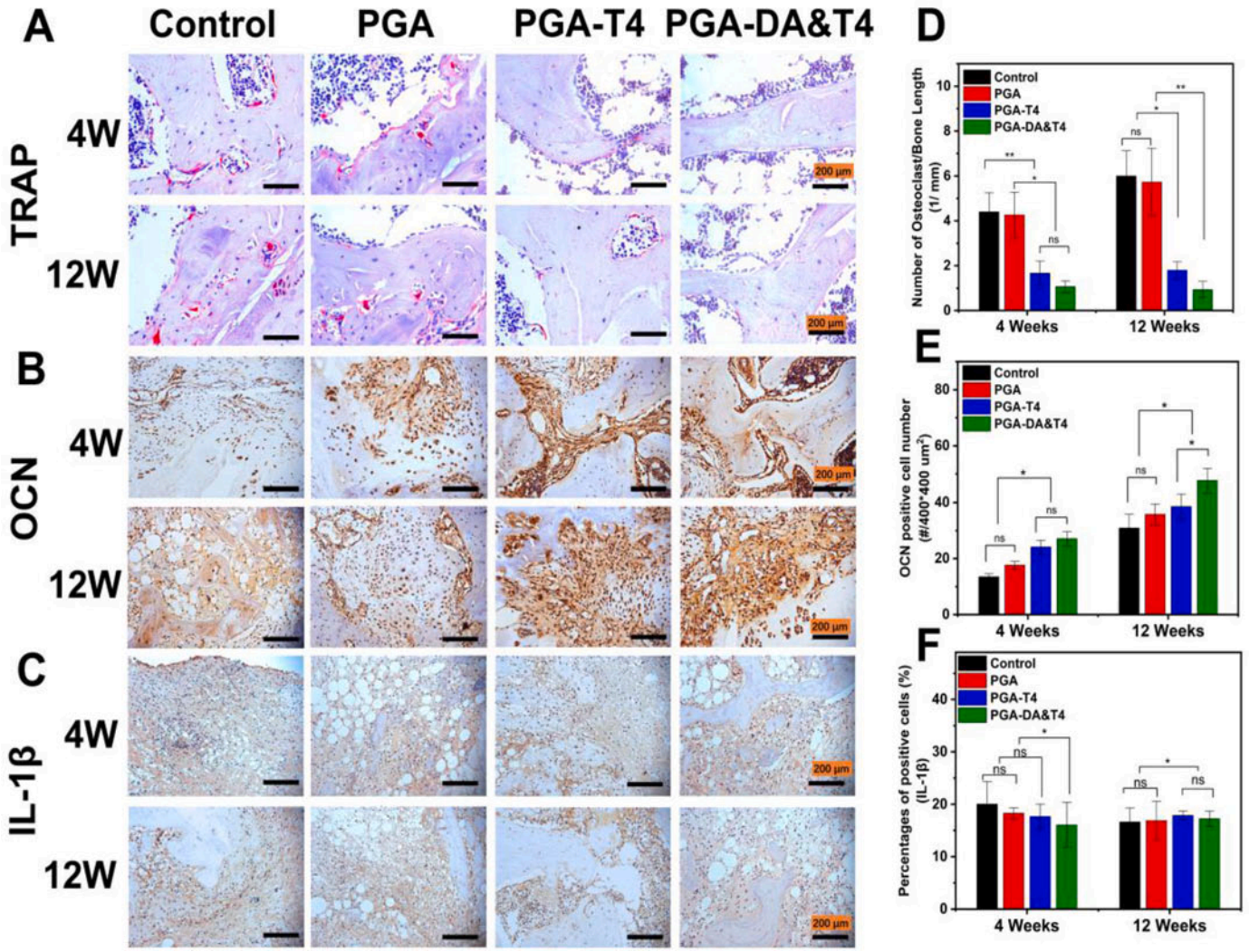

Fig. 8. Immunohistochemical staining images. Immunohistochemical staining images of A) TRAP, B) OCN, and C) IL-1β, and corresponding quantitative rsults of D) TRAP, E) OCN, and F) IL-1β for different samples 4 and 12 weeks postoperation. Data are presented as mean ± SD (n = 3). (scale bars 200um; *p < 0.05, **p < 0.01, ***p < 0.005).

Ethics approval and consent to participate

All animal experiments were conducted in compliance with the Animal Experimental Committee of Institute of Biological and Medical Engineering, Guangdong Academy of Sciences (Approval No. 2021013).

CRediT authorship contribution statement

Lingli Liu: Writing – review & editing, Writing – original draft, Validation, Supervision, Project administration, Methodology, Investigation, Funding acquisition, Formal analysis, Data curation, Conceptualization. **Shiyuan Ma:** Writing – original draft, Supervision, Methodology, Investigation, Formal analysis, Data curation. **Zhisheng Xiao:** Supervision, Methodology, Investigation, Formal analysis, Data curation. **Jintao Li:** Investigation, Formal analysis, Data curation. **Yue Wang:** Investigation, Formal analysis, Data curation. **Zhihui Lu:** Writing – review & editing, Project administration, Funding acquisition. **Yitao Zhao:** Writing – review & editing, Writing – original draft, Investigation, Formal analysis. **Jinshan Guo:** Writing – review & editing, Project administration, Funding acquisition.

Declaration of competing interest

The authors declare that they have no known competing financial interests or personal relationships that could have appeared to influence the work reported in this paper.

Data availability

No data was used for the research described in the article.

Acknowledgments

L. Liu, S. Ma, and Z. Xiao contributed equally to this work. This work was supported by the Youth Talent of Guangdong Special Support Program (0620220207), the Natural Science Foundation of China (Grant No. 82272453, U21A2099, and 82102545), the Chinese Post-doctoral Science Foundation (Grant No. 2023M731553), and the Open Program from Guangdong Provincial Key Laboratory of Bone and Joint Degeneration Disease.

Appendix A. Supplementary data

Supplementary data to this article can be found online at https://doi.org/10.1016/j.compositesb.2024.111713.

References

[1] Ayers C, Kansagara D, Lazur B, Fu R, Kwon A, Harrod C. Effectiveness and safety of treatments to prevent fractures in People with low bone mass or primary osteoporosis: a living systematic review and network meta-analysis for the American college of physicians. Ann Intern Med 2023;176(2):182–95.
[2] Zhang W, Zhou X, Hou W, Chen E, Ye C, Chen M, Lu Q, Yu X, Li W. Reversing the imbalance in bone homeostasis via sustained release of SIRT-1 agonist to promote bone healing under osteoporotic condition. Bioact Mater 2022;19:429–43.
[3] Lee J, Byun H, Sk Madhurakkat Perikamana, Lee S, Shin H. Current advances in immunomodulatory biomaterials for bone regeneration. Adv Healthcare Mater 2019;8(4):e1801106.
[4] Liang X, Yang X, Liu J, Chen Y, et al. ROS-scavenging bioactive scaffold orchestrates bone regeneration for osteoporotic bone defect repair. Compos B Eng 2024;281:111528.
[5] Deng J, Song Q, Liu, Liu S, et al. Advanced applications of cellulose-based composites in fighting bone diseases. Compos B Eng 2022;245:110221.
[6] Koons GL, Diba M, Mikos AG. Materials design for bone-tissue engineering. Nat Rev Mater 2020;5(8):584–603.
[7] Lei C, Song J, Li S, et al. Advances in materials-based therapeutic strategies against osteoporosis. Biomaterials 2023;296:122066.
[8] Mallick SP, Suman DK, Singh BN, et al. Strategies toward development of biodegradable hydrogels for biomedical applications. Polymer-Plastics Technology and Materials 2020;59(9):911–27.
[9] Xue X, Hu Y, Deng Y, et al. Recent advances in design of functional biocompatible hydrogels for bone tissue engineering. Adv Funct Mater 2021;31(19):2009432.
[10] Zheng Z, Yu C, Wei H. Injectable hydrogels as three-dimensional network reservoirs for osteoporosis treatment. Tissue Eng B Rev 2021;27(5):430–54.
[11] Stafin K, Śliwa P, Piątkowski M. Towards polycaprolactone-based scaffolds for alveolar bone tissue engineering: a biomimetic approach in a 3D printing technique. Int J Mol Sci 2023;24(22):16180.
[12] Haidar Z. S., Abdurakhmonov I. Y., Barkaoui A. Mechanobiological behavior of a pathological bone. Biomechanics and Functional Tissue Engineering. IntechOpen. Available at:https://doi.org/10.5772/intechopen.97029.
[13] Cheng S, H Wang K, Zhou L, et al. Tailoring biomaterials ameliorate inflammatory bone loss. Adv Healthcare Mater 2024:2304021.
[14] Kuang L, Huang J, Liu Y, Li X, Yuan Y, Liu C. Injectable hydrogel with NIR light-responsive, dual-mode PTH release for osteoregeneration in osteoporosis. Adv Funct Mater 2021;31(47):2105383.
[15] Gao J, Feng L, Chen B, et al. The role of rare earth elements in bone tissue engineering scaffolds-A review. Compos B Eng 2022;235:109758.
[16] Shokrani H, Shokrani A, Seidi F, et al. Artificial intelligence for biomedical engineering of polysaccharides: a short overview. Curr Opin Biomed Eng 2023;27:100463.
[17] Liu W, Huan Z, Wu C, et al. High-strength calcium silicate-incorporated magnesium phosphate bone cement with osteogenic potential for orthopedic application. Compos B Eng 2022;247:110324.
[18] Toosi S, Naderi-Meshkin H, Moradi A, Daliri M, Heirani-Tabasi A, Behravan J, et al. Scaphoid bone nonunions: clinical and functional outcomes of collagen/PGA scaffolds and cell-based therapy. ACS Biomater Sci Eng 2023;9(4):1928–39.
[19] Yang R, Xue W, Ma X, Chi B, et al. Engineering the dynamics of biophysical cues in supramolecular hydrogels to facile control stem cell chondrogenesis for cartilage regeneration. Compos B Eng 2023;250:110429.
[20] Zhang W, Song S, Huang J, et al. An injectable, robust double network adhesive hydrogel for efficient, real-time hemostatic sealing. Chem Eng J 2023;476:146244.
[21] Haag H, Dalton PD, Bloemen V. The synergy of biomimetic design strategies for tissue constructs. Adv Funct Mater 2022;32(32):2201414.
[22] Tamburaci S, Tihminlioglu F. Chitosan-hybrid poss nanocomposites for bone regeneration: the effect of poss nanocage on surface, morphology, structure and in vitro bioactivity. Int J Biol Macromol 2020;142:643–57.
[23] Zhong X, Wei G, Liu B, Guo H, et al. Polyhedral oligomeric silsesquioxane-based nanoparticles for efficient chemotherapy of glioblastoma. Small 2023;19(18):2207248.
[24] Wang M, Song Y, De Yoreo JJ, Chen CL, et al. Programmable two-dimensional nanocrystals assembled from POSS-containing peptoids as efficient artificial light-harvesting systems. Sci Adv 2021;7(20):eabg1448.
[25] Liu L, Xu T, Gui X, Gao S, Sun L, Lin Q, Song X, Wang Z, Xu K. Electrospun Silsequioxane-grafted PVDF hybrid membranes for high-performance rechargeable lithium batteries. Compos B Eng 2021;215:108849.
[26] Li D, Liu L, Song X, et al. Coupling silsesquioxane nanocages into Fe-Mg-Al layered metal hydroxide for enhanced flame retardancy and surface charring of silicone elastomer. Colloids Surf A Physicochem Eng Asp 2023;676:132156.
[27] Legnani L, Iannazzo D, Pistone A, et al. Functionalized polyhedral oligosilsesquioxane (POSS) based composites for bone tissue engineering: synthesis, computational and biological studies. RSC Adv 2020;10(19):11325–34.
[28] Zhao Y, Li J, Liu L, et al. Zinc-based tannin-modified composite microparticulate scaffolds with balanced antimicrobial activity and osteogenesis for infected bone defect repair. Adv Healthcare Mater 2023;12(20):2300303.
[29] Shan B, Wu F. Hydrogel-based growth factor delivery platforms: strategies and recent advances. Adv Mater 2023;36(5):2210707.
[30] Gao X, Zhang X, Zhang R, et al. Aggressive strategies for regenerating intervertebral discs: stimulus-responsive composite hydrogels from single to multiscale delivery systems. J Mater Chem B 2022;10(30):5696–722.
[31] Liu S, Guo R, Li C, et al. POSS hybrid hydrogels: a brief review of synthesis, properties and applications. Eur Polym J 2021;143:110180.
[32] Guo J, Tian X, et al. Citrate-based tannin-bridged bone composites for lumbar fusion. Adv Funct Mater 2020;30:2002438.
[33] Fu M, Zhao Y, et al. On-demand removable self-healing and pH-responsive europium-releasing adhesive dressing enables inflammatory microenvironment modulation and angiogenesis for diabetic wound healing. Small 2023;19(3):2205489.
[34] Wu M, Zhao Y, et al. Malate-based biodegradable scaffolds activate cellular energetic metabolism for accelerated wound healing. ACS Appl Mater Interfaces 2023;15(44):50836–53.
[35] Guo J, Wang W, Hu J, et al. Synthesis and characterization of anti-bacterial and anti-fungal citrate-based mussel-inspired bioadhesives. Biomaterials 2016;85:204–17.
[36] Guo J, Kim GB, Shan D, et al. Click chemistry improved wet adhesion strength of mussel-inspired citrate-based antimicrobial bioadhesives. Biomaterials 2017;112:275–86.
[37] Zhang M, Liu J, Zhu T, et al. Functional macromolecular adhesives for bone fracture healing. ACS Appl Mater Interfaces 2022;14(1):1–19.
[38] Wu K, Fu M, Zhao Y, et al. Anti-oxidant anti-inflammatory and antibacterial tannin-crosslinked citrate-based mussel-inspired bioadhesives faciliate scarless wound healing. Bioact Mater 2023;20:93–110.
[39] Lasisi KH, Yao W, Xue Q, Liu Q, Zhang K. High performance polyamine-based acid-resistant nanofiltration membranes catalyzed with 1,4-benzenecarboxylic acid in interfacial cross-linking polymerization process. J Membr Sci 2021;640:119833.
[40] Zou YP, Liang HF, Wang B, Zhang QC, Su DH, Lu SY, Zhang QY, Wu T, Xiao L, Xiao Y, Dong J, Jiang LB, Li XL. Precipitation-based silk fibroin fast gelling, highly

adhesive, and magnetic nanocomposite hydrogel for repair of irregular bone defects. Adv Funct Mater 2023;33(29):2302442.
[41] Vinikoor T, Dzidotor GK, Le TT, Liu Y, Kan H-M, Barui S, Chorsi MT, Curry EJ, Reinhardt E, Wang H, Singh P, Merriman MA, D'Orio E, Park J, Xiao S, Chapman JH, Lin F, Truong C-S, Prasadh S, Chuba L, Killoh S, Lee S-W, Wu Q, Chidambaram RM, Lo KWH, Laurencin CT, Nguyen TD. Injectable and biodegradable piezoelectric hydrogel for osteoarthritis treatment. Nat Commun 2023;14(1):6257.
[42] Wang W, Wei J, Lei D, et al. 3D printing of lithium osteogenic bioactive composite scaffold for enhanced bone regeneration. Compos B Eng 2023;256:110641.
[43] Koons GL, Diba M, Mikos AG. Materials design for bone-tissue engineering. Nat Rev Mater 2020;5(8):584–603.
[44] Hou Y, Jin M, Sun D, et al. Multifunctional inorganic/organic nanocomposite microspheres-reinventing eggs for bone repair applications. Compos B Eng 2023; 255:110644.
[45] Wang X, Gao L, Han Y, et al. Silicon-enhanced adipogenesis and angiogenesis for vascularized adipose tissue engineering. Adv Sci 2018;5(11):1800776.